International Journal for Numerical Methods in Biomedical Engineering

WILEY

SPECIAL ISSUE ARTICLE OPEN ACCESS

Uncertainty Quantification and Sensitivity Analysis for Non-invasive Model-Based Instantaneous Wave-Free Ratio Prediction

Caterina Dalmaso[1] | Fredrik Eikeland Fossan[2] | Anders Tjellaug Bråten[3,4] | Lucas Omar Müller[1]

[1]Department of Mathematics, University of Trento, Trento, Italy | [2]Department of Structural Engineering, Norwegian University of Science and Technology, Trondheim, Norway | [3]Clinic of Cardiology, St. Olavs Hospital, Trondheim, Norway | [4]Department of Circulation and Medical Imaging, Norwegian University of Science and Technology, Trondheim, Norway

Correspondence: Caterina Dalmaso (caterina.dalmaso@unitn.it; dalmaso0caterina@gmail.com)

Received: 10 October 2023 | **Revised:** 20 November 2024 | **Accepted:** 29 November 2024

Funding: This work was supported by Gruppo Nazionale per il Calcolo Scientifico. Norges Forskningsråd. Università degli Studi di Trento.

Keywords: 1D distributed stenosis model | 1D-0D model | coronary flow | instantaneous wave-free ratio | sensitivity analysis

ABSTRACT

The main objectives of this work are to validate a 1D-0D unsteady solver with a distributed stenosis model for the patient-specific estimation of resting haemodynamic indices and to assess the sensitivity of instantaneous wave-free ratio (iFR) predictions to uncertainties in input parameters. We considered 52 patients with stable coronary artery disease, for which 81 invasive iFR measurements were available. We validated the performance of our solver compared to 3D steady-state and transient results and invasive measurements. Next, we used a polynomial chaos approach to characterise the uncertainty in iFR predictions based on the inputs associated with boundary conditions (coronary flow, compliance and aortic/left ventricular pressures) and vascular geometry (radius). Agreement between iFR and the ratio between cardiac cycle averaged distal and aortic pressure waveforms (resting P_d / P_a) obtained through 1D-0D and 3D models was satisfactory, with a bias of 0.0–0.005 (±0.016–0.026). The sensitivity analysis showed that iFR estimation is mostly affected by uncertainties in vascular geometry and coronary flow (steady-state parameters). In particular, our 1D-0D method overestimates invasive iFR measurements, with a bias of −0.036 (±0.101), indicating that better flow estimates could significantly improve our modelling pipeline. Conversely, we showed that standard pressure waveforms could be used for simulations, since the impact of uncertainties related to inlet-pressure waveforms on iFR prediction is negligible. Furthermore, while compliance is the most relevant transient parameter, its effect on iFR estimates is negligible compared to that of vascular geometry and flow. Finally, we observed a strong correlation between iFR and resting P_d / P_a, suggesting that steady-state simulations could replace unsteady simulations for iFR prediction.

1 | Introduction

Obstructive coronary artery disease (CAD) is the most common manifestation of cardiovascular disease and one of the main mortality causes worldwide [1, 2]. It is characterised by the presence of atherosclerotic plaques in the epicardial coronary arteries [3] and can result in several clinical presentations. In this study, we consider patients with suspected chronic coronary syndromes (CCS): Coronary computed tomography angiography (CCTA) is the recommended test in symptomatic patients with low/intermediate likelihood of CAD, and several studies showed that it significantly reduces the number of patients referred to invasive procedures,

Abbreviations: CAD, coronary artery disease; CCTA, coronary computed tomography angiography; FFR, fractional flow reserve; iFR, instantaneous wave-free ratio; resting P_d/P_a, resting distal to aortic pressure ratio; UQ&SA, uncertainty quantification and sensitivity analysis.

with no increase in long term events [4–7]. Nonetheless, if intermediate grade stenoses are detected via CCTA scans, patients are commonly referred to a functional evaluation of lesions via haemodynamic indices such as fractional flow reserve (FFR) [8–10] and instantaneous wave-free ratio (iFR) [11–13], or directly to revascularisation procedures [14, 15]. Moreover, while FFR is currently regarded as the golden standard for the functional assessment of stenosis severity, iFR has been shown to be non-inferior in guiding revascularisation in two large clinical trials (DEFINE-FLAIR [16] and iFR-SWEDEHEART [17]), while being less costly and risky, as well as more versatile [18, 19]. These considerations motivate why clinicians are increasingly interested in the development of non-invasive methods that can provide an accurate assessment of the functional significance of stenoses by combining the geometrical information provided by CCTA scans with either machine learning or computational fluid dynamics and mathematical models. In this context, CCTA-derived FFR (FFR_{CT}) [20] has emerged as a tool to refer patients to invasive procedures [21–31], and the software by HeartFlow Inc. (Redwood City, California, United States of America) has been demonstrated as superior to measures of stenosis severity obtained through CCTA scans for determining lesion-specific ischemia [32]. These methods are based on some common general steps [33]: (i) definition of the computational domain; (ii) definition of an appropriate mathematical model to solve fluid mechanics in the computational domain; (iii) definition of boundary conditions; (iv) numerical solution of model equations and (v) computation of the index of interest. In this article, we follow this general pipeline to define a method for computational iFR estimation, since only few works are currently available to this end in the literature [34–39].

Liu et al. [34] proposed a closed-loop model for iFR estimation that couples a CCTA-derived 3D model of coronary arteries to 0D models of the heart, pulmonary and systemic circulations. Validation was performed with respect to 62 invasive FFR measurements, 9 of which with FFR below the critical threshold of 0.8 for revascularisation. The analysis reported in Ma et al. [36] was performed on a population of 33 patients (47 lesions, 17 with $FFR \leq 0.8$) and proved a strong correlation between computational iFR estimates obtained through 3D computational fluid dynamics (CFD) models and invasive FFR measurements. Finally, the analysis performed by Zhang et al. [35] on a population of 36 patients (36 vessels, 14 lesions with iFR below the critical threshold of 0.89 [40]) showed that iFR estimates obtained through deep learning and CFD-based models provided diagnostic indices comparable with those obtained with 3D models, using both invasively measured FFR and iFR values as reference.

The major downside of using 3D models for clinical purposes is their high computational cost, while the training of neural networks requires a sufficiently large pool of data. Consequently, in this work, we adopted a 1D-0D approach that couples a transient 1D description of blood flow within the main epicardial coronary arteries to 0D models of the coronary microcirculation. This choice allowed us to perform uncertainty quantification and sensitivity analysis (UQ&SA), which provided a crucial understanding of model errors and uncertainties in the modelling pipeline. A stenosis detection algorithm [33, 41] was used to separate healthy segments from stenotic segments. Blood flow description within healthy segments is similar to those proposed in Carson et al. [39] and Ge et al. [38, 42], differing from them mainly in the chosen boundary conditions and tube law. Pressure losses across stenoses were described, instead, through a novel 1D distributed stenosis model. The choice of using a transient model, which is computationally more expensive than steady-state ones, stems from the fact that iFR prediction requires an accurate characterisation of diastolic pressure decay, which cannot be obtained through steady-state simulations.

We performed a threefold validation of the proposed 1D-0D model. First, we considered 679 lesions identified by the stenosis detection algorithm, and we compared the estimates of the ratio between cardiac cycle averaged distal and aortic pressure waveforms (resting P_d / P_a) obtained through a 3D steady-state Navier Stokes solver and our unsteady 1D-0D model. Additionally, we compared iFR predictions obtained with an unsteady 3D Navier Stokes solver with 1D-0D iFR predictions obtained considering identical boundary conditions (prescribed inlet pressure waveform and 0D Mantero-Windkessel models at outlets). Finally, we compared 1D-0D iFR and resting P_d / P_a estimates to a set of 81 invasive measurements of the two indices. Several works have investigated the sensitivity of computational FFR predictions to parameter variations and modelling simplifying assumptions [41, 43–45], but, as far as we know, no analogous analysis has been performed for iFR yet. Motivated by this fact, we conducted a sensitivity analysis to assess the impact of uncertainties in six parameters related to the geometry of the computational domain and the prescribed boundary conditions on iFR predictions.

The rest of this paper is structured as follows. In Section 2, we describe the acquisition of patient-specific data (Section 2.1), a 1D-0D model for iFR prediction (Sections 2.2 and 2.3), the numerical methods employed to solve model equations (Section 2.4) and, finally, the methodology we employed to conduct uncertainty quantification and sensitivity analysis (Section 2.5). In Section 3, we present results for the validation of the 1D-0D model (Sections 3.1 and 3.2) and for the UQ&SA analysis performed on iFR predictions (Section 3.3). Finally, Section 4 includes a detailed discussion of our findings and in Section 5 we report future steps to be taken in order to reduce uncertainty in iFR predictions.

2 | Methods

2.1 | Patients and Data Acquisition

We consider a population of 52 patients, recruited as a part of an ongoing clinical trial at St. Olavs hospital, Trondheim, Norway [46]. The included patients had undergone invasive angiography and FFR/iFR measurement after clinical examinations and CCTA scans indicated stable CAD. For these patients, a total of 81 iFR measurements were collected, with mean 0.9 and standard deviation of 0.15. Positive iFR prevalence was 24.69% for a cutoff value of $iFR < 0.89$ [47]. Exclusion criteria included unstable CAD, nondiagnostic quality of the CCTA, previous revascularisation procedures, contraindications to adenosine, age (75 years or older) and obesity. See Table 1 for a summary of population characteristics.

Medical data was acquired as explained in [33, 41]. In particular, CCTA was performed using two CT scanners with 2×128 detector rows (Siemens dual source Definition Flash) and 256

TABLE 1 | Study population characteristics. Results are reported as "mean (standard deviation)" unless otherwise specified.

Characteristics	Units	Datum
Generic data		
No. of patients	—	52
No. of male patients	Datum (percentage)	32 (61.53)
Age	y	59.13 (7.81)
Height	cm	174.09 (9.60)
Weight	kg	86.26 (13.41)
Body mass index	kg/cm^2	28.4 (3.49)
Invasive MAP	mmHg	99.73 (13.45)
Cardiac output (ultrasound)	L/min	5.08 (0.89)
Cardiac output (Equation (24))	L/min	6.00 (1.15)
Left ventricular mass	g	154.17 (32.02)
Invasive iFR measurements		
iFR	—	0.9 (0.15)
iFR prevalence	Datum (percentage)	20/81 (24.69)
Measurement location		
LCA	Datum (percentage)	59/81 (72.84)
RCA	Datum (percentage)	22/81 (27.16)

Abbreviations: CAD, coronary artery disease; iFR, instantaneous wave-free ratio; LCA, left coronary artery (including its branches); RCA, right coronary artery.

detector row CT scanners (Revolution CT, GE Healthcare, Waukesha, Wisconsin, US) with a standardised protocol [48]. A commercial software (Syngo.via, Siemens, Germany) was used to quantify left ventricle mass (LVM) from CCTA scans. Echocardiographic imaging was performed using a GE Vivid E95 scanner (GE Vingmed Ultrasound, Horten, Norway). Cardiac output (CO) was computed based on the cross-sectional area of the left ventricle outflow tract (measured immediately proximal to the points of insertion of the aortic leaflets) and on the velocity time integral derived from PW Doppler. iFR was measured using Verrata Plus (Philips Volcano, San Diego, USA) pressure wires according to standard practice. Intra-coronary nitroglycerin (0.2 mg) was given to all patients before advancing the pressure wire into the coronary arteries. After measurement, the pressure wire was removed back to the equalisation point at the tip of the guiding catheter to ensure that there was no drift. Invasive pressure tracings were recorded during invasive coronary angiography and made available for further processing, while standard non-invasive diastolic/systolic pressure measurements were performed on both arms using an automatic, digital blood pressure device, Welch Allyn ProBP 3400.

Segmentation of coronary vessels was performed semi-automatically using the commercial software Mimics (Materialise's Interactive Medical Image Control System; Materialise, Leuven, Belgium). Surface mesh processing, addition of flow extensions and meshing were performed through the open-source library Vascular Modeling ToolKit (VMTK) [49]. To obtain the 1D domains used for the 1D-0D model simulations, centrelines were extracted from 3D domains through an algorithm available in VMTK, the portions of centrelines which correspond to arterial junctions were masked to exclude them from the 1D domain definition, and stenotic regions were identified. A detailed description of these steps is included in the works by Fossan et al. [41] and Müller et al. [33].

2.2 | 1D-0D Model

In this section, we present a transient 1D-0D model for iFR prediction that incorporates clinical imaging and patient-specific characteristics.

2.2.1 | Mathematical Model

Blood flow equations can be derived from the Navier–Stokes equations [50–52] and read as follows:

$$\begin{aligned} &\partial_t A + \partial_x(Au) = 0 && \text{mass conservation,}\\ &\partial_t(Au) + \partial_x\left(Au^2\right) + \frac{A}{\rho}\partial_x P = -R_v u && \text{momentum balance} \end{aligned} \tag{1}$$

where $A(x,t)$, $u(x,t)$ and $p(x,t)$ are the unknowns of the system (respectively the vessel cross-sectional area at position x and time t, the averaged velocity of blood at a cross section and the pressure), $\rho = 1.050\,\text{g/cm}^3$ is the density of blood and R_v is the viscous resistance of the flow per unit length of the tube. In healthy segments, we assume that $R_v = \frac{12.62\pi\mu}{\rho}$ [25, 41], with $\mu = 0.035$ dyne/cm^2, while its expression in stenotic tracts will be derived in Section 2.2.2. The system is closed with a tube law of the form

$$P = p_0 + \psi\left(A; A_0, K\right), \tag{2}$$

where $p_0 = 90$ mmHg is a constant reference pressure [50, 53, 54], and $\psi\left(A; A_0, K\right)$ is defined as

$$\psi\left(A; A_0, K\right) = K\left[\left(\frac{A(x,t)}{A_0(x)}\right)^{1/2} - 1\right]. \tag{3}$$

Here A_0 is the vessel cross-sectional area at equilibrium, which takes values derived from the segmentation of medical images, and the stiffness coefficient K is defined as

$$K = 2\rho c_0^2. \tag{4}$$

c_0 is the reference wave-speed for a vessel [55], which in turn is considered to be a function of the average A_0 along the considered vessel.

Developing the partial derivative of pressure, system (1) reads

$$\begin{aligned} &\partial_t A + \partial_x(Au) = 0,\\ &\partial_t(Au) + \partial_x\left(Au^2\right) + \frac{A}{\rho}\frac{\partial P}{\partial A}\partial_x A = -R_v u - \frac{A}{\rho}\frac{\partial P}{\partial A_0}\partial_x A_0. \end{aligned} \tag{5}$$

Following the procedure outlined in [53–57], A_0 can be incorporated within the model as a state variable, thus obtaining a non-conservative system which can be written in quasilinear form as

$$\partial_t \mathbf{Q} + \mathbf{A}(\mathbf{Q})\partial_x \mathbf{Q} = \mathbf{S}(\mathbf{Q}), \tag{6}$$

where

$$\mathbf{Q} = \begin{bmatrix} A(x,t) \\ Au(x,t) \\ A_0(x) \end{bmatrix}, \quad \mathbf{A}(\mathbf{Q}) = \begin{bmatrix} 0 & 1 & 0 \\ c^2 - u^2 & 2u & \frac{A}{\rho}\frac{\partial P}{\partial A_0} \\ 0 & 0 & 0 \end{bmatrix}, \quad \mathbf{S}(\mathbf{Q}) = \begin{bmatrix} 0 \\ -R_v u \\ 0 \end{bmatrix},$$

and $c = \sqrt{\frac{A}{\rho}\frac{\partial P}{\partial A}}$.

The eigenstructure of system (6) is that of its homogenised version and is given by the eigenvalues and associated eigenvectors of the coefficient matrix $\mathbf{A}(\mathbf{Q})$: $\lambda_1 = u - c$, $\lambda_2 = 0$, and $\lambda_3 = u + c$. A possible choice of right eigenvectors $\mathbf{R}_i, i = 1 \dots 3$, of $\mathbf{A}(\mathbf{Q})$ corresponding to the eigenvalues λ_1, λ_2, and λ_3 is the following [53]:

$$\mathbf{R}_1 = \begin{bmatrix} 1 \\ u - c \\ 0 \end{bmatrix}, \mathbf{R}_2 = \begin{bmatrix} \frac{A}{\rho}\frac{\partial P/\partial A_0}{u^2 - c^2} \\ 0 \\ 1 \end{bmatrix}, \mathbf{R}_3 = \begin{bmatrix} 1 \\ u + c \\ 0 \end{bmatrix}. \tag{7}$$

The definition of $\psi(A; A_0, K)$ we adopted for the tube law, reported in Equation (3), implies that the system (6) is strictly hyperbolic for $A \in \mathbb{R}_{>0}$, $u \in \mathbb{R}$ as long as $|u|$ is different from c. We will operate under the assumption of subcritical flow ($|u| < c$), so that this hypothesis will be satisfied. Moreover, it can be easily shown that the λ_1 and λ_3-characteristic fields are genuinely non-linear and, consequently, associated to shocks and rarefactions, while the λ_2-characteristic field is linearly degenerate and associated with a stationary contact discontinuity. Furthermore, genuine non-linearity allows the definition of the generalised Riemann invariants associated to the system [53]. In particular, the generalised Riemann invariants for the λ_1 and λ_3 characteristic field are, respectively, $A_0 = \text{const}$, $\int \frac{c(A)}{A} dA + u = \text{const}$ and $A_0 = \text{const}$, $\int \frac{c(A)}{A} dA - u = \text{const}$, while the generalised Riemann invariants for the λ_2-characteristic field are

$$Au = \text{const}, \quad \frac{1}{2}\rho u^2 + P = \text{const}. \tag{8}$$

Equation (8) implies that both flow and total pressure are preserved across the stationary contact discontinuity determined by the discontinuity in reference cross-sectional area A_0.

Regions masked as bifurcations are not modelled through a continuous model. Instead, centreline nodes belonging to junctions are collapsed into a single point, where we enforce mass conservation (9a) and continuity of total pressure (9b):

$$\sum_{i=1}^{N} q_i = 0, \tag{9a}$$

$$P_1 + \frac{\rho}{2}u_1^2 = P_i + \frac{\rho}{2}u_i^2, \qquad i = 2, \dots, N. \tag{9b}$$

where N is the number of vessels sharing a vertex with the bifurcation and $q = Au$ is the flow rate within a vessel.

2.2.2 | Distributed Stenosis Model

1D blood flow equations are not able to correctly describe the pressure drop across a stenosis since the assumptions under which they were derived do not hold in regions of flow separation such as downstream a stenosis [41]. To account for both viscous losses and terms related to flow separation, various approaches have been proposed.

Here, we chose to adapt the 1D stenosis models proposed by Steele et al. [58] and Jin et al. [59], which are derived under the assumption of constant flow rate and constant stenotic area, to the description of real stenoses with highly variable cross-sectional areas. Consider the experimentally derived stenosis model presented in Young et al. [60] and reformulated equivalently in Liang et al. [61]:

$$\Delta P = \frac{K_v \mu}{A_d D_d} q + \frac{K_t \rho}{2A_d^2}\left(\frac{A_d}{A_s} - 1\right)^2 q|q|, \tag{10}$$

where A_d and A_s refer to cross-sectional areas of healthy and stenotic segments and D_d is the healthy vessel diameter. The healthy radius was computed as $r_d = 0.5(r_u + r_d)$, where r_u and r_d are the radii immediately upstream and downstream the stenosis, while the stenotic radius was assumed to be the minimum radius along the stenosis [41]. K_t and K_v are empirically determined coefficients and $q = Au$ is the volumetric flow rate across the stenosis. The coefficient $K_t = 1.52$ is independent of the stenosis geometry and represents losses caused by the formation of vortices due to the sudden expansion of the stenosis. K_v describes viscous losses that dominate at low Reynolds numbers. It was shown experimentally [62] that this coefficient depends on the length of the stenosis L_s and on the diameters of the healthy and stenotic segments D_d and D_s, and can be computed as

$$K_v = 32(0.83L_s + 1.64D_s)\frac{A_d^2}{A_s^2}\frac{1}{D_d}. \tag{11}$$

It is worth noting that the original ΔP reported in Young et al. [60] depends also on the time derivative of the flow rate. The authors solve the resulting ODE for the flow rate at each time step under the assumption that the pressure drop at the previous time step is available, obtaining a flow rate that is then prescribed in the last computational cell of the vessel proximal to the stenosis and in the first cell of the vessel distal to the stenosis. We chose to neglect this time-dependent term under the simplifying assumption of constant flow, which we made consistently with the approach by Steele et al. [58] due to its significant advantages for the numerical treatment of the problem. For completeness, we refer to the first section of the Supporting Information for a comparison between the pressure drops obtained with the unsteady 0D stenosis model by Young et al. [60] and its steady-state version.

Following the procedure outlined by Steele et al. [58], we can incorporate the pressure drop formulation in Equation (10) into our model through the loss term R_v in the momentum conservation equation. In particular, under the constant flow rate assumption ($\partial_t q = 0$ and $\partial_x q = 0$), we can manipulate the momentum balance equation in system (1) to isolate the spatial derivative of pressure $\partial_x P$, and obtain that

$$\partial_x P = -R_v \rho \frac{q}{A^2} + \rho \frac{q^2}{A^3} \partial_x A. \tag{12}$$

This equation can be integrated in space along the stenosis to obtain the pressure drop ΔP across the lesion:

$$\Delta P = P_L - P_R = \frac{\rho q^2}{2} \left(\frac{1}{A_{s,R}^2} - \frac{1}{A_{s,L}^2} \right) + R_v \rho q \int_{x_L}^{x_R} \frac{1}{A^2} dx, \tag{13}$$

where x_L and x_R are the left and right stenotic boundaries, $P_L = P(x_L)$ and $P_R = P(x_R)$ are the corresponding pressures, and $A_{s,L}$ and $A_{s,R}$ are the corresponding stenotic areas. Since the area is not constant, we notice that the pressure drop is dependent on the integral of the square of its inverse over the stenosis and, consequently, on the shape of the lesion.

Through a simple substitution one obtains

$$\begin{aligned} R_v = K_v \frac{\mu}{\rho} \frac{1}{A_d D_d} \frac{1}{\int_{x_L}^{x_R} \frac{1}{A^2} dx} + \frac{K_t}{2A_d^2} \left(\frac{A_d}{A_s} - 1 \right)^2 \frac{|q|}{\int_{x_L}^{x_R} \frac{1}{A^2} dx} \\ - \frac{1}{2} \left(\frac{1}{A_{s,R}^2} - \frac{1}{A_{s,L}^2} \right) \frac{q}{\int_{x_L}^{x_R} \frac{1}{A^2} dx}. \end{aligned} \tag{14}$$

This coefficient was then precomputed through Simpson's rule using a reference radius $r_{\text{geom}}(x)$ associated to the geometry of each employed network to evaluate

$$\begin{aligned} &A = \pi r_{\text{geom}}(x)^2, \quad A_{s,L} = \pi r_{\text{geom}}(x_L)^2, \quad A_{s,R} = \pi r_{\text{geom}}(x_R)^2, \\ &D_d = 2 \frac{r_{\text{geom}}(x_L) + r_{\text{geom}}(x_R)}{2}, \quad D_s = 2 \min_x \left(r_{\text{geom}}(x) \right). \end{aligned} \tag{15}$$

We can notice that for stenoses with constant areas and equal $A_{s,R}$ and $A_{s,L}$ we would obtain, from Equation (13), $\Delta P = R_v \rho q L_s / A_s^2$ and, consequently,

$$R_v = \frac{\Delta P}{\rho} \frac{A_s^2}{q L_s}, \tag{16}$$

which is exactly the coefficient reported in Steele et al. [58].

2.2.3 | Boundary Conditions

In this work, we performed both steady-state simulations prescribing a constant pressure at the inlet of the network and constant flow rates $\hat{q}_{out}^j$, $j = 1, \ldots, N_{out}$ at its outlets, and unsteady simulations prescribing a time-dependent pressure waveform at the inlet of the network and coupling lumped parameter models to its outlets. The details on parameter definition are illustrated in Section 2.3.

2.2.3.1 | Lumped Parameter Models Coupled to Outlets. Coronary blood flow is determined both by aortic pressure and by the pressure variations that arise distally from an active compression and decompression of the coronary microcirculation caused by the rhythmic contraction and relaxation of the myocardium [11]. This motivates the choice of coupling network outlets to 0D models derived from the work by Mantero et al. [63], which account for coronary arterial and venous resistance, for the resistances of coronary arterial and venous microcirculation, for coronary arterial and left ventricular compliance and for the time varying left ventricular pressure. A schematic representation of this model setup is shown in Figure 1. The variation in volume V within each compartment of the lumped parameter model is described by the ODE system

$$\frac{dV_{p,j}}{dt} = q_{out,j} - \frac{P_{p,j} - P_{m,j}}{R_{m,j}}, \tag{17}$$

$$\frac{dV_{m,j}}{dt} = \frac{P_{p,j} - P_{m,j}}{R_{m,j}} - \frac{P_{m,j} - P_{d,j}}{R_{d,j}}, \tag{18}$$

where $q_{out,j}$ is the flow exiting the j-th 1D domain and entering the lumped parameter model, P and R represent pressure and resistance of different components of the lumped model, and the subscripts p, m and d stand respectively for proximal, medial and distal. $q_{out,j}$ can be computed through Ohm's law as

$$q_{out,j} = \frac{p_{out,j} - P_{p,j}}{R_{p,j}}, \tag{19}$$

where $p_{out,j}$ is the pressure at the inlet of the lumped parameter model. Volumes and pressures are related via compliance C through equations

$$P_{p,j} = \frac{V_{p,j}}{C_{p,j}}, \tag{20}$$

$$P_{m,j} = \frac{V_{m,j}}{C_{m,j}} + P_{LV}, \tag{21}$$

where P_{LV} is the left ventricular pressure. ODEs (17) and (18) are solved through a fourth-order Runge–Kutta method, as proposed by [64].

2.3 | Computational iFR Estimation Pipeline

Assuming that a patient-specific dataset is available, the pipeline for the 1D-0D model iFR prediction is the following:

1. Define 1D domain from CCTA scans of patients through segmentation, meshing and post-processing procedures.
2. Define baseline coronary flow q_{branch} through an appropriate strategy [33]. Here, we chose to estimate stroke volume (SV) from non-invasively measured patient-specific parameters, which are normally acquired during the diagnostic procedure for CAD, using the formula originally proposed in de Simone et al. [65]

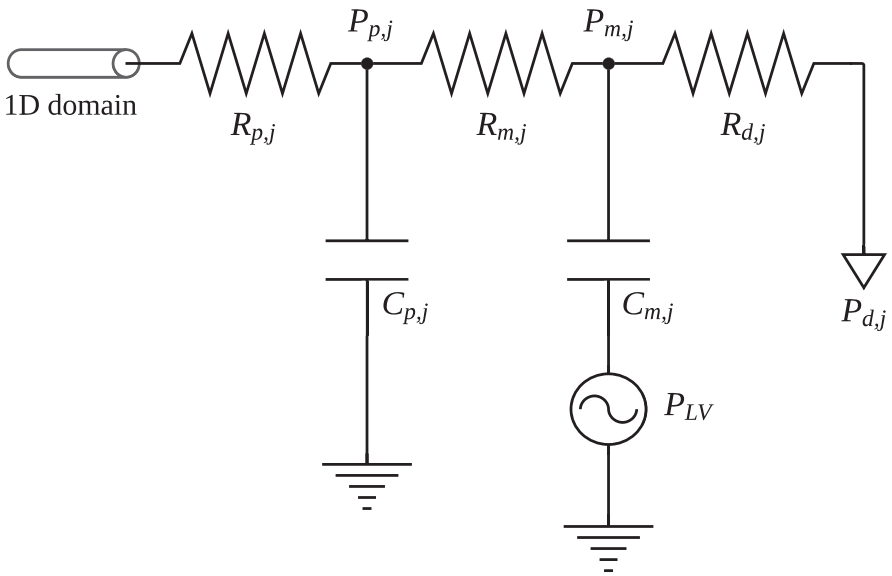

FIGURE 1 | Schematic representation of a lumped-parameter model couplet to the j-th 1D domain outlet. C denotes compliances, R resistances and P pressures, while the subscripts p, m and d stand for proximal, medial and distal, respectively. P_{LV} denotes the time-varying left ventricular pressure.

TABLE 2 | Distributions of total arterial compliance according to Halushka et al. [68] and of λ_{cor} according to Sakamoto et al. [66].

Parameter	Branch, dominance	Symbols	Baseline value	Distributions
Total arterial compliance	—	C_{TOT} [mL mmHg^{-1}]	1.2	$\mathcal{N}(1.2,0.48)$
Coronary flow fraction	Left, right	$\lambda_{\text{cor}}(\%)$	2.6	$\mathcal{U}(1.78,3.42)$
Coronary flow fraction	Right, right	$\lambda_{\text{cor}}(\%)$	1.9	$\mathcal{U}(1.1,2.7)$
Coronary flow fraction	Left, left	$\lambda_{\text{cor}}(\%)$	3.4	$\mathcal{U}(2.7,4.1)$
Coronary flow fraction	Right, left	$\lambda_{\text{cor}}(\%)$	0.9	$\mathcal{U}(0.27,1.6)$

$$SV = PP^* \times [(0.013 \times W) - (0.007 \times Y) - (0.004 \times HR) + 1.307] \tag{22}$$

where W is the weight in kilograms, Y is the age in years, HR the heart rate in beats per minute. PP^* is computed as

$$PP^* = (0.49 \times PP) + (0.3 \times Y) + 7.11 \tag{23}$$

where the pulse pressure PP is defined as the difference between systolic and diastolic blood pressures (in mmHg). Then, the cardiac output (CO) is computed as

$$CO = HR \times SV \tag{24}$$

The estimation of baseline coronary flow to a specific coronary branch was based on the work by Sakamoto et al. [66]:

$$q_{branch} = \lambda_{cor} CO \tag{25}$$

where the values for λ_{cor} depend on the considered branch and on the patients' coronary arterial dominance and are reported in Table 2.

3. Model validation versus 3D simulations was conducted splitting the flow q_{branch} among the network's N_{out} outlets through the vessel length-based flow-distribution method used for 3D simulations [67].

For model validation versus invasive measurements and UQ&SA, instead, we chose to split the flow q_{branch} according to the following relationship based on vessel radius.

$$q^j_{\text{out}} = q_{\text{branch}} \frac{(\text{mean}r_j)^3}{\sum_{i=1}^{N_{out}} (\text{mean}r_j)^3}, \qquad j = 1, \ldots, N_{\text{out}} \tag{26}$$

where $\text{mean}r_j$ denotes the average radius of the j-th terminal vessel.

4. Perform a steady-state simulation with prescribed inlet pressure P_{root}, equal to the cardiac cycle average of the invasively measured patient-specific aortic pressure and prescribed outlet flows q^j_{out} defined in previous step. Compute resistances at outlets [33] as

$$R_{\text{out},j} = \frac{P_{\text{out},j} - P_v}{q^j_{\text{out}}}, \text{with } j = 1, \ldots, N_{\text{out}} \tag{27}$$

Here, $P_{\text{out},j}$ denotes the pressure value at the j-th outlet obtained through the steady-state simulation, and $P_v = 5$ mmHg is a reference venous pressure.

5. Perform a transient simulation with aortic pressure waveform $P_{\text{in}}(t)$ at the inlet of the vascular network and prescribed

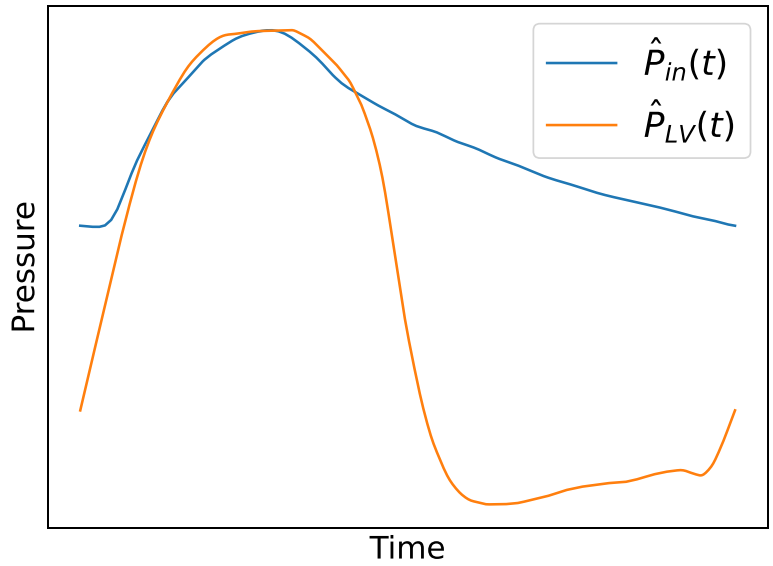

FIGURE 2 | Aortic (blue) and left ventricle (orange) template waveforms used for patient-specific simulations.

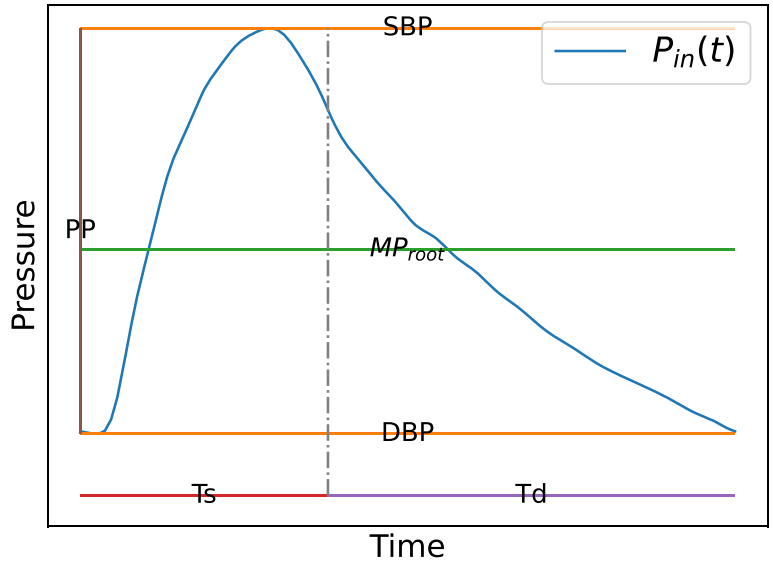

FIGURE 3 | Aortic pressure waveform parametrised in terms of pulse pressure, mean arterial pressure, cardiac cycle and systole duration.

lumped parameter models at outlets. Aortic pressure was computed scaling a population-based template pressure waveform $\widehat{P}_{\text{in}}(t)$ (Figure 2) in terms of cardiac cycle-averaged pressure MP_{root}, pulse pressure (PP), cardiac cycle duration and systole to cardiac cycle duration ratio (Figure 3). These quantities were extracted from pressure tracings for aortic pressure acquired during invasive iFR measurement. We employed the lumped-parameter models presented in Section 2.2.3, which are parametrised in terms of resistances, compliances and left ventricular pressure. The considered resistances were those computed in the previous step, while coronary peripheral compliance was obtained splitting the total arterial compliance by Halushka et al. [68] according to the flow percentages by Sakamoto et al. [66] (see Table 2). Coronary peripheral compliance C_{branch} was distributed among outlets using Murray's law [69]

$$C_{\text{out},j} = C_{\text{branch}} \frac{r_j^3}{\sum_{i=1}^{N_{\text{out}}} r_j^3}, \qquad j = 1, \ \dots, N_{\text{out}} \tag{28}$$

where j stands for the j-th outlet of the network. Resistances $R_{\text{out},j}$ and compliances $C_{\text{out},j}$ were subsequently distributed among the different compartments of the lumped parameter model attached to the j-th outlet (see Figure 1). The fractions used for distributing $R_{\text{out},j}$ among $R_{p,j}$, $R_{m,j}$ and $R_{d,j}$ were set, respectively, to 0.01, 0.84 and 0.15, while those used to distribute $C_{\text{out},j}$ among $C_{p,j}$ and $C_{m,j}$ are 0.025 and 0.975, respectively [41]. Similarly to aortic pressure, left ventricular pressure $P_{LV}(t)$ was computed from a template pressure waveform $\widehat{P}_{LV}(t)$ (Figure 2), scaled in terms of systolic blood pressure, cardiac cycle duration and systole duration.

Simulation results obtained through step 5 represent the state from which iFR and resting P_d / P_a can be evaluated at any point of the network. In particular,

$$iFR^j_{1D-0D} = \frac{\int_{\text{WFP}} P_{\text{dist},j}(t)dt}{\int_{\text{WFP}} P_{\text{in}}(t)dt} \tag{29}$$

where *WFP* denotes the diastolic wave-free period [11], which is defined from 25% of the diastolic length into the diastolic phase to 15% of the diastolic length before the end of the cardiac cycle [70], and $P_{\text{dist},j}(t)$ is the predicted pressure at the j-th node of the network. Resting P_d / P_a, instead, is defined as

$$\text{resting}P_d / P_a{}^{j}_{1D-0D} = \frac{\int_T P_{\text{dist},j}(t)dt}{\int_T P_{\text{in}}(t)dt}, \tag{30}$$

where T denotes cardiac cycle duration.

2.4 | Numerical Methods: MUSCL-Hancock Finite Volume-Type Scheme

System (1) cannot be cast in conservative form [54] and, consequently, classical finite volume schemes based on the finite volume formula cannot be employed for its solution due to the presence of non-conservative products [71]. Several implicit, semi-implicit and explicit approaches have been proposed in the literature to deal with this type of problems. Particularly relevant explicit methods are the finite element [72–74], finite volume [56, 75] and finite difference [76, 77] methods [78, 79]. As far as implicit and semi-implicit methods are concerned, we mention here the simplified trapezoidal rule method [80, 81], unconditionally stable fully implicit methods based on the finite element [82, 83] and finite volume [84, 85] frameworks and semi-implicit flux splitting schemes [86, 87].

For this work, we built a MUSCL-Hancock type [88] second-order well-balanced scheme based on a first-order path-conservative scheme and on a well-balanced high-order reconstruction operator [89, 90]. To achieve this, we chose to depart from the second-order method developed in Spilimbergo et al. [54] and modified it to preserve well-balancing for steady flows in vessels characterised by marked variations in cross-sectional area. MUSCL-Hancock finite volume schemes are fully discrete methods obtained solving a generalised Riemann problem at each cell interface through a spatial reconstruction step, the evolution of the so-called boundary extrapolated values and the solution of a classical Riemann problem. Here, the reconstruction and evolution steps were based on the theory introduced in Müller et al. [90], and the solution of the classical Riemann problem at the interface was obtained through the non-conservative DOT solver [91]. Compared to the method proposed by Spilimbergo et al. [54], we chose to perform spatial reconstruction on deviations around a hypothetical steady-state solution, and we expressed the second component of non-conservative products in terms of total pressure. In addition, we computed the first component $\overline{A}(s)$ of the path used to solve the classical Riemann problem by inverting the segment path for total pressure. In the following, after a brief explanation of employed notation, we report our changes to the method described in Spilimbergo et al. [54] and refer to Section 2 of the Supporting Information for a full description of the scheme.

Consider the control volume $V_i^n = \left[x_{i-\frac{1}{2}}, x_{i+\frac{1}{2}}\right] \times \left[t^n, t^{n+1}\right]$ and integrate (6) using integration by parts [56, 57] to obtain

$$\mathbf{Q}_i^{n+1} = \mathbf{Q}_i^n - \frac{\Delta t^n}{\Delta x}\left(\mathbf{D}^-_{i+\frac{1}{2}} + \mathbf{D}^+_{i-\frac{1}{2}}\right) - \mathbf{G}_i + \Delta t^n \mathbf{S}_i, \tag{31}$$

where $\mathbf{Q}_i^n \simeq \frac{1}{\Delta x}\int_{x_{i-\frac{1}{2}}}^{x_{i+\frac{1}{2}}} \mathbf{Q}(t^n, x)\text{dx}$ is the approximation of the average of the exact solution at the i-th computational cell at time level t^n, the non-conservative product $\mathbf{G}_i$ is the approximation of the time integral of the spatial average of the product between the coefficient matrix and the spatial partial derivative of the state vector $\mathbf{G}_i \simeq \frac{1}{\Delta x}\int_{t^n}^{t^{n+1}} \int_{x_{i-1/2}}^{x_{i+1/2}} \mathbf{A}(\mathbf{Q})\partial_x \mathbf{Q}\text{dxdt}$, the numerical source $\mathbf{S}_i$ is defined as the approximation of the spatial–temporal integral average of the source term at the i-th computational cell $\mathbf{S}_i \simeq \frac{1}{\Delta t^n \Delta x}\int_{t^n}^{t^{n+1}} \int_{x_{i-1/2}}^{x_{i+1/2}} \mathbf{S}(\mathbf{Q}(x,t))\text{dxdt}$, and $\mathbf{D}^{\pm}_{i+\frac{1}{2}} = \mathbf{D}^{\pm}\left(\mathbf{Q}_L, \mathbf{Q}_R, \Psi\right)$ with $\mathbf{Q}_L$, $\mathbf{Q}_R$ respectively the states at the left and right of cell interface $x_{i+\frac{1}{2}}$. $\mathbf{D}^-\left(\mathbf{Q}_L, \mathbf{Q}_R, \Psi\right)$ and $\mathbf{D}^+\left(\mathbf{Q}_L, \mathbf{Q}_R, \Psi\right)$, which are called numerical fluctuations, are two Lipschitz continuous path-dependent functions that have to satisfy $\mathbf{D}^{\pm}(\mathbf{Q}, \mathbf{Q}, \Psi) = 0$ over the considered domain and $\mathbf{D}^-\left(\mathbf{Q}_L, \mathbf{Q}_R, \Psi\right) + \mathbf{D}^+\left(\mathbf{Q}_L, \mathbf{Q}_R, \Psi\right) = \int_0^1 \mathbf{A}\Psi\left(\mathbf{Q}_L, \mathbf{Q}_R, s\right)\frac{\partial \Psi}{\partial s}\left(\mathbf{Q}_L, \mathbf{Q}_R, s\right)\text{ds}$ for every $\mathbf{Q}_L$, $\mathbf{Q}_R$ [56, 71, 92].

The following paragraphs will describe in detail data reconstruction, our approach to deal with non-conservative products and the path we employed to solve the classical Riemann problem arising from the MUSCL framework.

2.4.1 | Spatial Reconstruction

Appropriate data reconstruction methods allow to obtain high order of accuracy. In particular, to obtain second order of accuracy, one can choose appropriate piecewise linear functions, which are defined through their slopes $\Delta^n_{k,i}$:

$$p^n_{k,i} = Q^n_{k,i} + \left(x - x_i\right)\Delta^n_{k,i}, \tag{32}$$

where Q_k, $k = 1, \ldots, m$ denotes the $k-th$ component of the state vector and i denotes the considered computational cell. A common choice of reconstruction operator is the ENO criterion [93]. We focus here on the reconstruction for the cross-sectional area, due to the fact that a modification of the ENO reconstruction operator was necessary to preserve well-balanced properties of the high-order scheme [90], since steady solutions of system (6) may not be polynomials. We employed a spatial reconstruction algorithm whose output, in the presence of a steady solution, is a polynomial that is equal to the steady solution at cell interfaces. In particular, for computational cell I_i, the procedure is the following:

1. Perform ENO reconstruction on the stencil $S_i = \left\{I_i, I_{i-1}, I_{i+1}\right\}$ for the flow component of the state vector Q to obtain polynomials (32).
2. Recall the generalised Riemann invariants for the λ_2 -characteristic field defined in Equation (8). Compute the roots of $A^n_i = \frac{1}{2}\left(A\left(x_{i-\frac{1}{2}}, q_{i-\frac{1}{2}}, \Gamma^*_i\right) + A\left(x_{i+\frac{1}{2}}, q_{i+\frac{1}{2}}, \Gamma^*_i\right)\right)$ to find a total pressure value

$$\Gamma^*_i = \frac{1}{2}\rho u^{*2} + P^* \tag{33}$$

such that the cell average A^n_i of the cross-sectional area at time n is equal to the average of the area values $A\left(x_{i\pm\frac{1}{2}}, q_{i\pm\frac{1}{2}}, \Gamma^*_i\right)$ we would obtain at the left and right

cell interfaces $x_{i\pm\frac{1}{2}}$ in steady-state conditions. Area values are expressed as functions of space, Γ_i^* and flow values $q_{i\pm\frac{1}{2}} = Q_{2,i}^n + \left(x_{i\pm\frac{1}{2}} - x_i\right)\Delta_{2,i}^n$, where $\Delta_{2,i}^n = 0$ in steady-state conditions. We note that the aforementioned Riemann invariant always exists and is unique under the assumption of subcritical flow.

3. Once the Riemann invariant Γ_i^* is available, for every cell j belonging to the stencil S_i compute

$$\mathcal{V}_j^n = A_j^n - \frac{1}{2}\left(A\left(x_{j-\frac{1}{2}}, q_{j-\frac{1}{2}}, \Gamma_i^*\right) + A\left(x_{j+\frac{1}{2}}, q_{j+\frac{1}{2}}, \Gamma_i^*\right)\right),$$

which measures the deviation of the cell averages A_j^n from the steady-state solutions found at the previous step.

4. Apply ENO reconstruction to the deviations $\mathcal{V}_j^n$ to obtain an auxiliary slope $\mathcal{D}_{A,i}^n$ for the cross-sectional area, which is null in case of steady-state solutions, and compute the final ENO slope for the cross-sectional area as

$$\Delta_{1,i}^n = \frac{1}{\Delta x}\left(A\left(x_{i+\frac{1}{2}}, q_{i+\frac{1}{2}}, \Gamma_i^*\right) - A\left(x_{i-\frac{1}{2}}, q_{i-\frac{1}{2}}, \Gamma_i^*\right)\right) + \mathcal{D}_{A,i}^n. \quad (34)$$

2.4.2 | Non-conservative Products in the Evolution Procedure

Non-conservative products are present in Equation (31) ($\mathbf{G}_i$) and arise in the evolution of boundary extrapolated values (reconstruction polynomials evaluated at cell interfaces) required by the MUSCL framework. The treatment of the two cases is analogous. Let us define any non-conservative product $\mathbf{NC}_i$ arising on the i-th computational cell from the procedure as a function of the non-conservative operator $\mathbf{nc}()$: $\mathbf{NC}_i = \Delta t\ \mathbf{nc}\left(\mathbf{Q}_i^n, \mathbf{\Delta}_i\right)$ with $\mathbf{\Delta}_i$ appropriate approximation of the spatial derivative of the state vector $\mathbf{Q}_i^n$. Normally, one would compute $\mathbf{NC}_i$ as the matrix–vector product $\mathbf{NC}_i = \mathbf{A}\left(\mathbf{Q}_i\right)\mathbf{\Delta}_i$, with $\mathbf{A}(\mathbf{Q})$ coefficient matrix of the system and $\mathbf{\Delta}_i = \frac{\mathbf{Q}_i^R - \mathbf{Q}_i^L}{\Delta x}$. Nonetheless, the second component of this product would require the use of $\Delta_{1,i} = \frac{A_i^R - A_i^L}{\Delta x}$, which is not exactly computed, since the cross-sectional area that solves the steady problem might not be a polynomial. As a consequence, we reformulate the second component of the non-conservative operator as

$$\mathrm{nc}_A\left(\mathbf{Q}_i, \mathbf{\Delta}_i\right) = \frac{q_i}{A_i}\Delta_{2,i} + \frac{A_i}{\rho}\frac{P_{\mathrm{TOT}}^R - P_{\mathrm{TOT}}^L}{\Delta x}, \quad (35)$$

where $P_{TOT}^k = P_i^k + \frac{1}{2}\rho\left(\frac{q_i^k}{A_i^k}\right)^2$, with $k = \{L, R\}$. Clearly, when considering steady-state solutions, $\Delta_{2,i} = 0$ and $\frac{P_{TOT}^R - P_{TOT}^L}{\Delta x} = 0$.

2.4.3 | Integration Path

The computation of numerical fluctuations $\mathbf{D}_{i+\frac{1}{2}}$ requires the solution of a classical Riemann problem at cell interface $x_{i+\frac{1}{2}}$. We chose to use the DOT solver for non-conservative systems [91, 94]:

$$\mathbf{D}_{i-\frac{1}{2}}^+ = \frac{1}{2}\sum_{j=1}^{4}\omega_j\left(\mathbf{A}\left(\Psi\left(\mathbf{Q}_{i-1}^R, \mathbf{Q}_i^L, s_j\right)\right) + \left|\mathbf{A}\left(\Psi\left(\mathbf{Q}_{i-1}^R, \mathbf{Q}_i^L, s_j\right)\right)\right|\right)\left.\frac{\partial\Psi}{\partial s}\right|_{s_j} \mathrm{ds}, \quad (36)$$

$$\mathbf{D}_{i+\frac{1}{2}}^- = \frac{1}{2}\sum_{j=1}^{4}\omega_j\left(\mathbf{A}\left(\Psi\left(\mathbf{Q}_i^R, \mathbf{Q}_{i+1}^L, s_j\right)\right) - \left|\mathbf{A}\left(\Psi\left(\mathbf{Q}_i^R, \mathbf{Q}_{i+1}^L, s_j\right)\right)\right|\right)\left.\frac{\partial\Psi}{\partial s}\right|_{s_j} \mathrm{ds}, \quad (37)$$

where ω_j and s_j are, respectively, the weights and Gaussian point coordinates of the considered quadrature rule. $\Psi(s)$ is a path that links in phase space the right and left states $\mathbf{Q}^L$ and $\mathbf{Q}^R$ in the Riemann problem, and $|\mathbf{A}| = \mathbf{R}|\mathbf{\Lambda}|\mathbf{R}^{-1}$, with $\mathbf{R}$ matrix of right eigenvectors for system (6) and $|\mathbf{\Lambda}|$ diagonal matrix of the corresponding eigenvalues of $\mathbf{A}$ in absolute value. We employed a variation of the integral path presented in Müller et al. [56], analogous to that proposed by Caleffi and Valiani for shallow water equations [95], which uses the segment path for all state variables except for the cross-sectional area and preserves steady-state solutions exactly:

$$\Psi_A\left(\mathbf{Q}_L(t), \mathbf{Q}_R(t), s\right) = \overline{A}(s) = \overline{\psi}(s)^{-1} \text{ for } 0 \le s \le 1, \quad (38)$$

where $\mathbf{Q}_L$ and $\mathbf{Q}_R$ are the left and right states to the considered cell interface. $\overline{\psi}(s)$ can be defined in terms of total pressure as

$$\overline{\psi}(s) = p_{TOT,L} + s\left(p_{TOT,R} - p_{TOT,L}\right). \quad (39)$$

Since total pressure is a function of area, $\overline{A}(s)$ can be computed through a globally convergent Newton's method.

The derivative $\left.\frac{\partial\Psi_A}{\partial s}\right|_{s_j}$ of $\Psi_A\left(\mathbf{Q}_L(t), \mathbf{Q}_R(t), s\right)$, required to compute the fluctuations through Equation (36), was computed as

$$\left.\frac{\partial\Psi_A}{\partial s}\right|_{s_j} = \left(\left(p_R - p_L\right) - \left.\frac{\partial\overline{\psi}}{\partial\overline{A}_0}\right|_{s_j}\left(A_{0,R} - A_{0,L}\right) - \left.\frac{\partial\overline{\psi}}{\partial\overline{q}}\right|_{s_j}\left(q_R - q_L\right)\right)\left(\left.\frac{\partial\overline{\psi}}{\partial\overline{A}}\right|_{s_j}\right)^{-1}. \quad (40)$$

2.5 | Uncertainty Quantification and Sensitivity Analysis

Patient-specific models use personalised inputs which may or may not be acquired in a clinical setting, and whose measurement is characterised by a high degree of uncertainty related to measurement errors and a large biological variability. Furthermore, clinical applicability of such models requires a fast response, meaning that they usually rely on simplified versions of the original physical problem, introducing further uncertainties. As a consequence, it is fundamental to understand the sensitivity of model predictions to uncertainties in model inputs to guide model design and to verify how uncertainties impact the accuracy of model outputs. The sensitivity of FFR predictions to various sources of uncertainty such as lesion geometry, peripheral resistances, blood viscosity, coronary flow fraction and stenosis parameters has been thoroughly investigated [41, 43–45, 96]. A similar extensive analysis of the sensitivity of iFR predictions to parameter variations and to modelling simplifying assumptions has not been performed yet and the results obtained for steady-state FFR models may not be directly extended to unsteady iFR models.

In this study, we performed three UQ&SA cases using a polynomial chaos approach. First, we assessed the sensitivity of computational iFR estimates to parameters that impact the steady-state portion of the pipeline described in Section 2.3 (segmented radius,

baseline coronary flow and mean arterial pressure). Subsequently, we assessed the uncertainty deriving from parameters used to parametrise the aortic pressure waveform and Mantero's lumped parameter models prescribed as boundary conditions in the unsteady portion of the pipeline (coronary arterial compliance, pulse pressure and duration of systole relative to the cardiac cycle). Finally, we combined the most relevant parameters identified through the previous analyses to assess whether iFR estimates are influenced more by steady-state or transient parameters, in order to determine whether it would be reasonable to estimate iFR through less computationally expensive steady-state simulations.

2.5.1 | Parameter Distributions

This section illustrates how we determined realistic parameter distributions for the three analyses we conducted. Considered parameters are the segmented radius (r), baseline coronary flow (q_{branch}), mean aortic and pulse pressures (respectively P_{root} and PP), the duration of systole relative to the cardiac cycle (T_s/T) and coronary arterial compliance (C_{branch}).

2.5.1.1 | Distributions for Parameters Related to Pressure. Distributions describing uncertainties in P_{root}, PP and T_s/T were computed using invasively measured aortic pressure waveforms for 63 patients. In particular, we chose to characterise uncertainties in P_{root} and PP through multipliers subsequently applied to the baseline patient-specific quantity

$$X_{\text{UQSA}} = X_{\text{base}} \cdot \Delta X \text{ for } X = P_{\text{root}}, PP,$$

where X_{UQSA} denotes the parameter value used for simulations and X_{base} is its baseline value. Distributions for these multipliers were obtained dividing data by their mean, identifying and removing outliers from the population to reduce the chance of obtaining parameter combinations resulting in supercritical simulations. Finally, we fitted a normal distribution to the obtained data. We thus obtained normal distributions centred approximately in 1, with standard deviation independent on the mean. For T_s/T, instead, we used the best normal distribution centred in the population mean and used samples from this distribution directly as parameters for simulations.

2.5.1.2 | Distribution for Baseline Coronary Flow. Uncertainty in coronary flow q_{branch} was characterised through a multiplier Δq_{branch} applied to a patient-specific baseline flow estimated through de Simone method (see Step 1 of the pipeline presented in Section 2.3)

$$q_{\text{branch,UQSA}} = q_{\text{branch,base}} \cdot \Delta q_{\text{branch}},$$

The distribution for Δq_{branch} was computed coupling population data and modelling results. We employed data pertaining to 18 coronary branches to compute baseline branch flows through the four methods illustrated in Müller et al. [33]:

$$\text{de Simone: } q_{\text{branch,dS}} = \lambda_{\text{cor}} \cdot CO_{\text{dS}}, \tag{41}$$

$$\text{Ultrasound: } q_{\text{branch,US}} = \lambda_{\text{cor}} \cdot CO_{\text{US}}, \tag{42}$$

$$\text{Kishi-Molina: } q_{\text{branch,KM}} = \beta \cdot 2.4 \cdot LVM, \tag{43}$$

$$\text{Sharma-¬Molina: } q_{\text{branch,SM}} = 0.14 \cdot (0.7 \cdot HR \cdot SBP \cdot 0.001 - 0.4) \cdot 2.4 \cdot LVM \cdot \frac{\lambda_{\text{cor}}}{0.045}, \tag{44}$$

where CO_{dS} is defined through Equations (22–24) CO_{US} is the cardiac output derived from patient-specific ultrasound measurements, $\beta = 0.8$ mL/min/g is a reference value for myocardial tissue perfusion, HR and SBP are, respectively, the heart rate and systolic blood pressure of patients and LVM is the left ventricular mass estimated from the CCTA scans of patients. In particular, we generated a set of samples for each method through python library chaospy employing population-based and literature-based parameter distributions. Datasets for each patient were then combined, and, after dividing data by their mean and removing outliers, we fitted the best normal distribution to the resulting dataset.

2.5.1.3 | Distribution for Coronary Arterial Compliance. Coronary arterial compliance C_{branch} can be computed as a percentage of total arterial compliance C_{TOT}

$$C_{\text{branch}} = C_{\text{TOT}} \cdot \lambda_{\text{cor}}, \tag{45}$$

with λ_{cor} flow fraction to a specific coronary branch. Its distribution was defined combining the uncertainties in C_{TOT} and λ_{cor} reported in Table 2 [66, 68], and generating a population-based dataset to which we fitted a uniform distribution after excluding outliers and negative compliance values.

2.5.1.4 | Distribution for Segmented Radius. To account for uncertainties in lumen cross-section, we applied a parameter $\Delta r \sim \mathcal{U}(-0.15, 0.15)$ to the radii in the network so that $r = r_s \cdot (1 + \Delta r)$, where r_s is the segmented radius.

A summary of the employed distributions is collected in Table 3, while the histograms of the normal distributions are reported in Figure 4.

2.5.2 | Uncertainty Quantification and Sensitivity Analysis Procedure

To conduct our sensitivity analysis, we followed the approach used by Fossan et al. [41], which is based on the review of Eck et al. [45]. Sensitivity of each model prediction to input uncertainties was assessed in terms of first-order and total Sobol sensitivity indices [45], computed here through the chaospy [97] implementation of the pseudo-spectral projection method, which is a non-intrusive polynomial chaos expansion method. Since both indices are based on scalar variables and in this work we considered multiple iFR estimates, we chose to summarise their sensitivities through average first-order (AS_i) and total ($AS_{T,i}$) Sobol sensitivity indices and through uncertainty weighted first-order (WS_i) and total ($WS_{T,i}$) sensitivity indices [41]. We can summarise the employed procedure for UQ&SA as follows.

1. Identify the model output of interest $\mathcal{Y}$ and approximate the joint distribution $\rho_{\mathbf{Z}}$ of the input random vector $\mathbf{Z}$.
2. Define a set of numerical quadrature nodes $S_s = \{\mathbf{z}^{(s)}\}_{s=1}^{N_s}$ in parameter space $\Omega_{\mathbf{Z}}$ and a set of associated quadrature

TABLE 3 | Input uncertainties for the assessment of the effects of parametric input uncertainty on 1D-0D estimates of iFR.

Input	Source of baseline value	Symbols	Distribution
Pulse pressure	Invasive aortic pressure tracings	ΔPP	$\mathcal{N}(0.98,0.27)$
Mean aortic pressure	Invasive aortic pressure tracings	ΔP_{root}	$\mathcal{N}(0.99,0.09)$
Systole over cardiac cycle duration	Population average	T_s / T	$\mathcal{N}(0.38,0.06)$
Flow entering the coronary branch	de Simone et al. [65], Sakamoto et al. [66]	Δq_{branch}	$\mathcal{N}(0.99,0.30)$
Coronary arterial compliance	Population average	C_{branch} [mL/mmHg]	$\mathcal{U}\left(1.14 \cdot 10^{-3},0.071\right)$
Segmented radius	CCTA-derived segmentation	Δr	$\mathcal{U}(-0.15,0.15)$

Note: Uniform distributions are denoted by $\mathcal{U}$ (min, max) and normal distributions by $\mathcal{N}$ (mean, std. dev.).

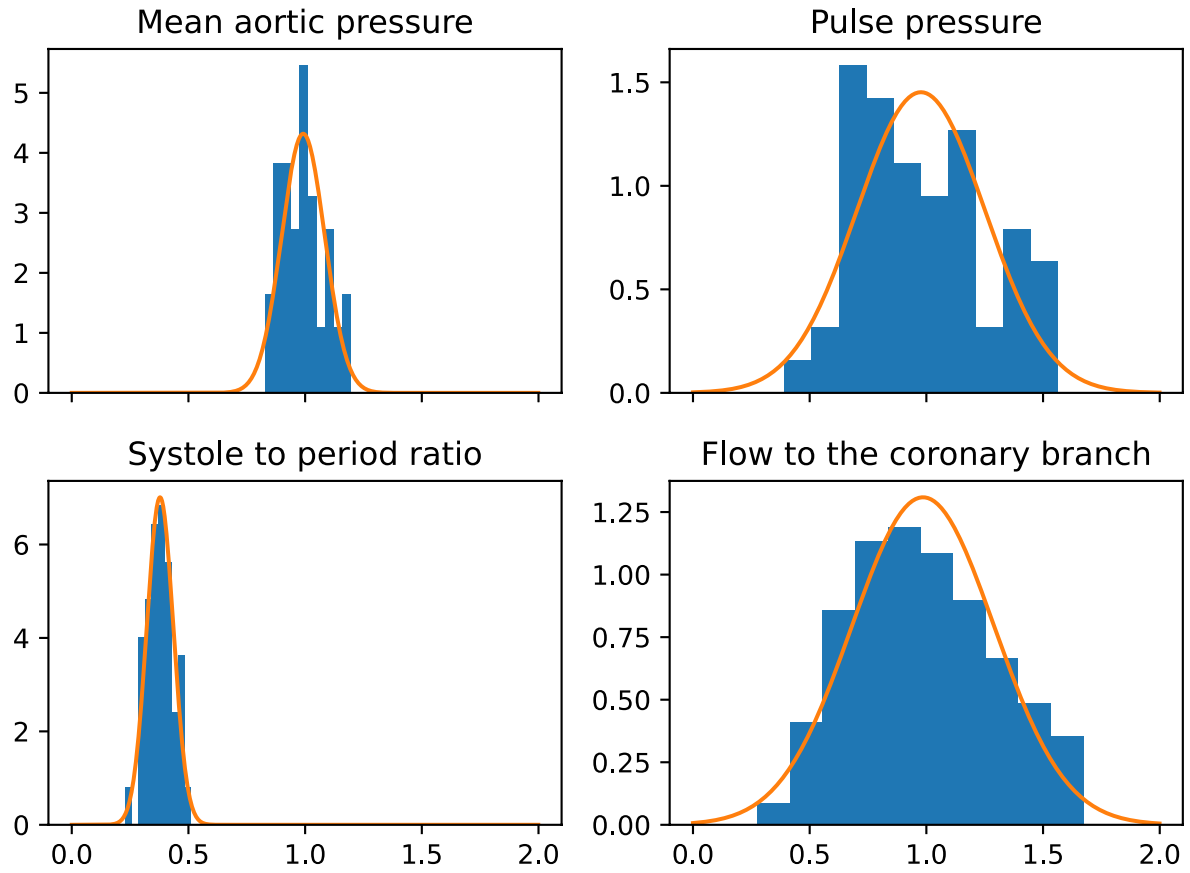

FIGURE 4 | Distributions of systole over cardiac cycle duration ratio and of the multipliers for mean aortic pressure, pulse pressure and baseline coronary flow.

weights $W_s = \left\{w^{(s)}\right\}_{s=1}^{N_s}$. We employed a Smolyak sparse-grid with optimal Gaussian quadrature rule. In particular, the chosen quadrature rule is a nested one, so that nodes of lower accuracy levels are employed for higher accuracy rules, allowing to use deterministic simulation results obtained at a lower accuracy level when moving to the next one.

3. Evaluate the deterministic model at quadrature nodes to obtain model evaluations $\mathcal{Y}_s = \left\{y^{(s)}\right\}_{s=1}^{N_s}$.
4. Select an expansion of orthogonal polynomials Φ_α. The order of polynomials was set equal to the accuracy level of the quadrature rule.
5. Estimate expansion coefficients c_α and construct the truncated polynomial chaos expansion

$$\hat{\mathcal{Y}} = \sum_{\alpha \in \Lambda} c_\alpha \Phi_\alpha(\mathbf{Z}). \tag{46}$$

6. Compute uncertainty and sensitivity measures through the approximation $\hat{\mathcal{Y}}$ and assess their convergence. The accuracy of UQ&SA results was assessed comparing the estimates obtained considering successive quadrature levels until the difference between estimated first-order and total Sobol sensitivity indices was below 0.02 for all indices with estimated value greater than 0.05. Approximation of maximum order 5 was performed, which required 355 simulations.

Further details are found in the fourth section of the Supporting Information.

3 | Results

3.1 | Validation of the 1D-0D Model Versus 3D Simulations

The proposed 1D-0D model was validated on a population of 52 patients, for a total of 40 left and 21 right coronary arteries. We performed a first comparison between 679 resting P_d/P_a estimates obtained with our 1D-0D solver and using a 3D steady-state Navier–Stokes solver. Furthermore, we compared iFR estimates obtained with our unsteady 1D-0D solver to 43 iFR predictions by an unsteady 3D Navier Stokes solver for a set of 28 patients (the first 28 recruited patients). The two comparisons were performed as follows:

1. 1D-0D results obtained performing step 4 of the pipeline illustrated in Section 2.3 versus 3D steady-state estimates. For 1D simulations, we prescribed the 3D steady-state pressure at the inlet of the network and 3D steady-state flows at its outlets.
2. 1D-0D results obtained through step 5 of the pipeline illustrated in Section 2.3 versus 3D unsteady estimates. For our 1D-0D simulations, we prescribed the same inlet pressure waveform employed for the 3D unsteady simulations, which we obtained by scaling a template aortic pressure waveform in terms of patient specific pulse pressure, mean arterial pressure and cardiac cycle duration. Moreover, we parametrised terminal lumped parameter models in terms of the cardiac-cycle averaged resistances resulting from the 3D unsteady simulations.

See Section 3 of the Supporting Information for details regarding the setup used for the three-dimensional simulations.

Figure 5 shows scatter plots and Bland–Altman plots for the two aforementioned scenarios. A numerical characterisation of these comparisons is provided in the top two rows of Table 4: we report the bias between the haemodynamic indices obtained through the 3D and 1D-0D models, coefficients for linear fitting and Pearson correlation coefficient, and we evaluate the diagnostic agreement

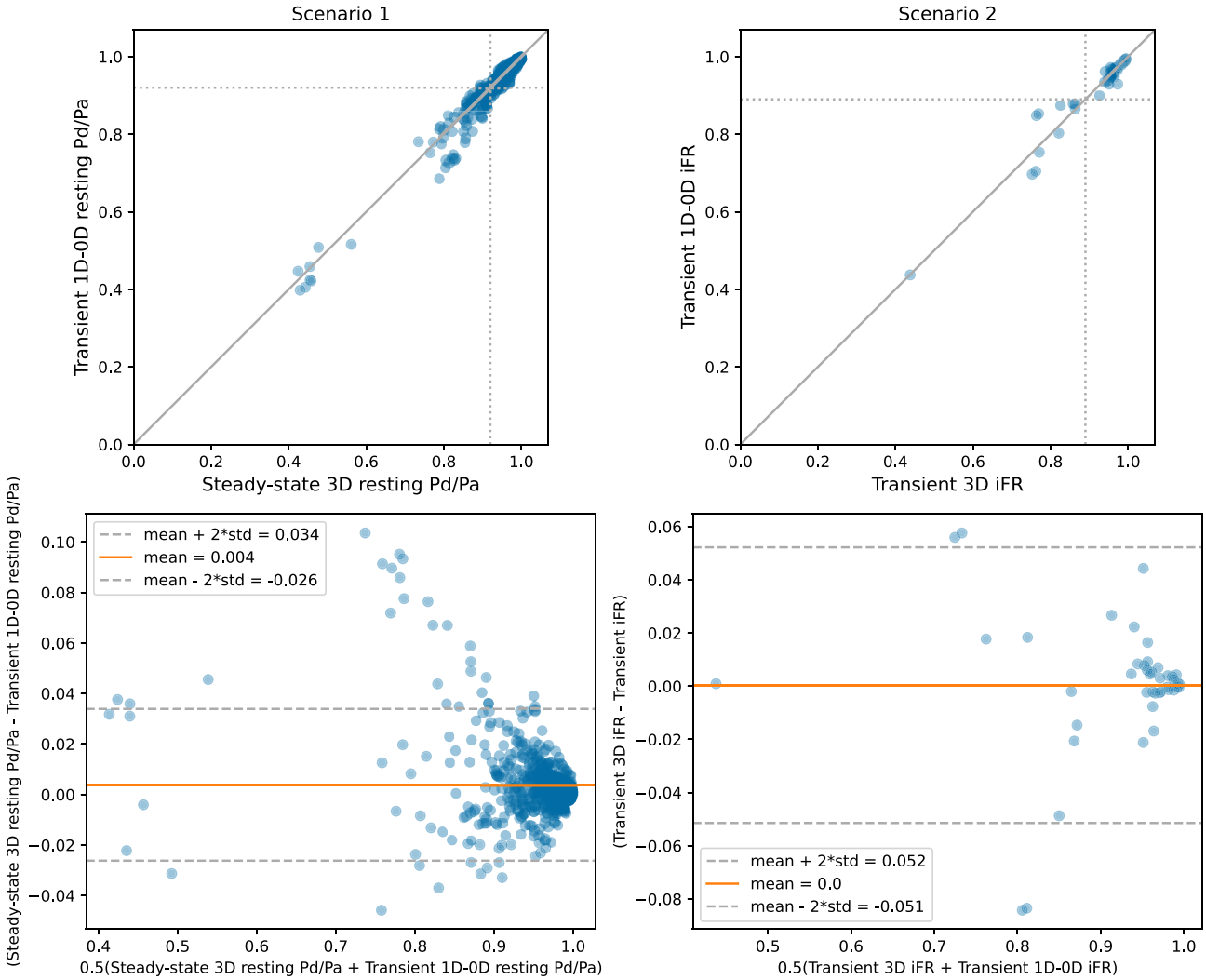

FIGURE 5 | Scatter plot and Bland–Altman plot of 1D-0D to steady-state 3D resting P_d/P_a, and of 1D-0D to unsteady 3D iFR (scenarios 1 and 2 in Section 3.1). The left column depicts results for the first scenario, which is characterised by a bias (difference between 3D and 1D-0D estimates) of 0.004 and a standard deviation of 0.015, whereas in the right column, we report results relative to the second scenario, for which we can observe a bias of 0.0 and a standard deviation of 0.026.

TABLE 4 | Comparison of (1) resting P_d/P_a obtained through steady-state 3D and unsteady 1D-0D models (scenario 1, Section 3.1), (2) iFR estimates obtained through transient 3D and 1D-0D models (scenario 2, Section 3.1) and (3) comparison of 1D-0D iFR and invasive iFR and (4) comparison of 1D-0D resting P_d/P_a and invasive resting P_d/P_a.

Comparison type	*a*	*b*	*r*	Bias	Acc.	Sens.	Spec.	PPV	NPV
1D-0D versus 3D estimates: scenario 1 (resting P_d/P_a)	1.05	−0.05	0.98	0.004 (0.015)	96.61	93.27	97.22	85.84	98.76
1D-0D versus 3D estimates: scenario 2 (iFR)	0.97	0.03	0.97	0.0 (0.026)	97.67	100.0	96.88	91.67	100.0
1D-0D versus invasive resting P_d/P_a	0.4	0.58	0.79	−0.02 (0.067)	82.72	57.14	91.67	70.59	85.94
1D-0D versus invasive iFR	0.37	0.6	0.8	−0.036 (0.101)	83.95	60.0	91.8	70.59	87.5

Note: *a* and *b* are coefficients for linear fitting, *r* is Pearson correlation coefficient. The bias was computed subtracting the 1D-0D estimate to the corresponding 3D (or invasive) one. Considered iFR and resting P_d/P_a critical thresholds are, respectively, 0.89 and 0.92 [40, 47]. Results are reported as mean (standard deviation).

in terms of accuracy, sensitivity, specificity, positive and negative predictive values (PPV and NPV, respectively).

3.2 | Validation Versus Invasive Measurements

Further model validation was performed comparing 81 1D-0D estimates of iFR and resting P_d/P_a, obtained using baseline patient-specific parameters (see Section 2.3 for their definition), to corresponding invasive measurements. Considered iFR and resting P_d/P_a critical thresholds for functionally significant lesions are, respectively, 0.89 and 0.92 [40, 47]. The bottom two rows of Table 4 collect a numerical characterisation of the diagnostic performance of the 1D-0D computational indices with respect to invasive measurements.

3.3 | Sensitivity Analysis

We performed three sensitivity analyses as illustrated in Section 2.5 to identify the most influential parameters for optimisation to guide model design.

3.3.1 | Uncertainty in Steady-State Parameters

This analysis was performed with respect to the uncertain input parameters $\mathrm{Z}_{\mathrm{iFR}} = \left[\Delta r, \Delta P_{\mathrm{root}}, \Delta q_{\mathrm{branch}}\right]$ at 81 locations where iFR was measured invasively, following the procedure illustrated in Section 2.5.2. Convergence of the first-order and total Sobol sensitivity indices was obtained within 4 accuracy levels for the considered 81 locations, requiring at most 168 simulations for each coronary branch. Average first-order and total Sobol sensitivity indices are visualised in Figure 6 (top row) together with weighted first-order and total sensitivity indices and reported in Table 5 (Analysis 1).

3.3.2 | Uncertainty in Transient Parameters

This analysis was performed with respect to the uncertain input parameters $\mathrm{Z}_{\mathrm{iFR}} = \left[C_{\mathrm{branch}}, T_s/T, \Delta PP\right]$ at 81 locations where iFR was measured invasively. Convergence of the first-order and total Sobol sensitivity indices was obtained at all locations within 5 quadrature levels, requiring at most 355 simulations for each coronary branch. Average first-order and total sensitivity indices are visualised in Figure 6 (second row) together with weighted first-order and total sensitivity indices and reported in Table 5 (Analysis 2).

3.3.3 | Uncertainty in the Most Relevant Parameters Identified by the Previous Analyses

This analysis was performed with respect to the uncertain input parameters $\mathrm{Z}_{\mathrm{iFR}} = \left[\Delta r, C_{\mathrm{branch}}, \Delta q_{\mathrm{branch}}\right]$ at 81 locations where iFR was measured invasively. Convergence of the first-order and total Sobol sensitivity indices was obtained within 4 accuracy levels, requiring at most 168 simulations for each coronary branch. Average first-order and total sensitivity indices are visualised in Figure 6 (bottom row) together with weighted first-order and total sensitivity indices and reported in Table 5 (Analysis 3).

3.3.4 | Impact of Parameter Uncertainty on iFR Prediction

Following the three analyses, we assessed the impact of uncertainties in the three considered sets of parameters on the relationship between iFR, which is computed averaging aortic and distal pressures over the diastolic wave-free period, and resting P_d/P_a, which is a cardiac-cycle averaged quantity that can be computed equivalently through steady-state and unsteady simulations [41]. Figure 7 shows scatter plots comparing resting P_d/P_a and iFR estimates obtained through our 1D-0D model for all parameter combinations considered for the three sensitivity analyses. Given the low observed scatter, we employed the linear relationship between resting P_d/P_a and iFR estimates reported in the plot on the bottom right

$$iFR = 1.24 \cdot \mathrm{resting} P_d/P_a - 0.24, \tag{47}$$

as a correction factor for resting P_d/P_a. Numerical results assessing the quality of this correction are reported in Table 6.

Furthermore, we compared average predicted iFR at each location and corresponding invasive measurements, highlighting the uncertainty in our estimates deriving from the variation of parameters considered for each analysis. Figure 8 shows the scatter plots for this comparison, where vertical error bars represent the 95% prediction intervals.

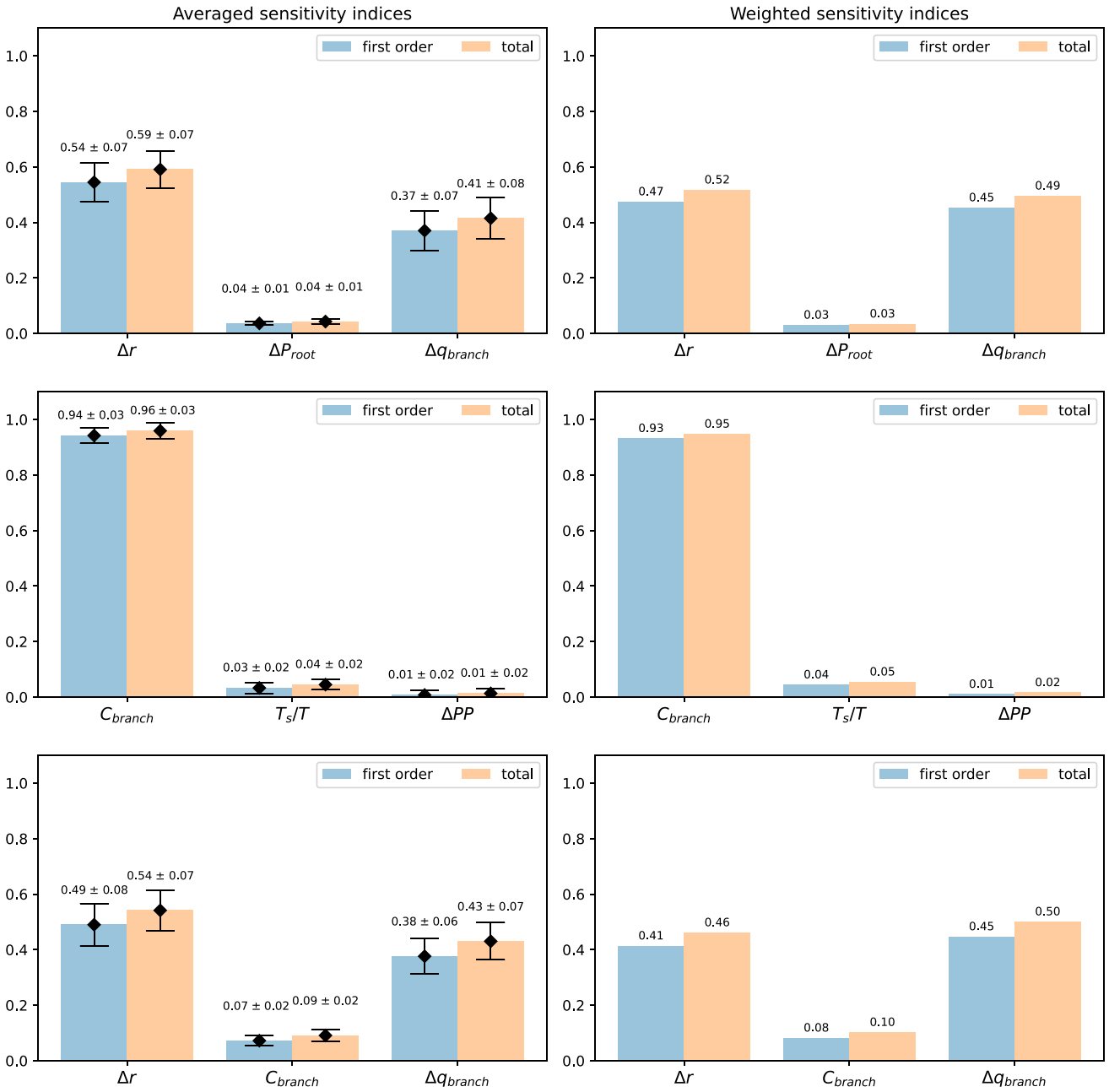

FIGURE 6 | Average first-order and total sensitivity indices, as well as weighted first-order and total sensitivity indices are reported for the three considered analyses. The first and second rows report, respectively, results obtained through the sensitivity analysis for steady-state and transient parameters. The third row shows results obtained through the analysis performed considering uncertainties in the most influential parameters identified through the previous analyses. Vertical black error bars denote the standard deviation of the average first-order and total sensitivity indices.

4 | Discussion

4.1 | Validation of the 1D-0D Model Versus 3D Simulations

In this study, we proposed a modelling framework for computational iFR estimation based on the use of a transient 1D-0D blood flow model. A stenosis detection algorithm [33, 41] was employed to separate stenotic segments from healthy segments. Blood flow in healthy segments was modelled using the 1D equations for blood in axisymmetric arteries, while the relation between pressure and flow in stenotic regions was described by a 1D model which includes viscous and convective terms from the 0D experimentally derived stenosis-model by Young et al. [98]. The models for healthy and stenotic segments were parametrised through clinical imaging and patient-specific characteristics.

We validated step 4 of our 1D-0D modelling pipeline against 3D steady-state simulations for 679 lesions detected by the stenosis detection algorithm by comparing resting P_d / P_a estimates obtained through the two models. Additionally, we validated the ability of the proposed 1D-0D model to capture relevant transient and pulsatile dynamics by comparison against 3D transient simulations for 43 stenoses. Diagnostic indices reported in Table 4 were computed under the assumption that the critical threshold for resting P_d / P_a is 0.92 and that the corresponding critical threshold for iFR is 0.89

TABLE 5 | Summary of sensitivities resulting from the three proposed analyses, which account respectively for uncertainties in steady-state, transient and most relevant parameters.

	Analysis 1			Analysis 2			Analysis 3		
	Δr	ΔP_{root}	Δq_{branch}	C_{branch}	T_s / T	ΔPP	Δr	C_{branch}	Δq_{branch}
AS_i	0.54 (0.07)	0.04 (0.01)	0.37 (0.07)	0.94 (0.03)	0.03 (0.02)	0.01 (0.02)	0.49 (0.08)	0.07 (0.02)	0.38 (0.06)
$AS_{T,i}$	0.59 (0.07)	0.04 (0.01)	0.41 (0.08)	0.96 (0.03)	0.04 (0.02)	0.01 (0.02)	0.54 (0.07)	0.09 (0.02)	0.43 (0.07)
WS_i	0.47	0.03	0.45	0.93	0.04	0.01	0.41	0.08	0.45
$WS_{T,i}$	0.52	0.03	0.49	0.95	0.05	0.02	0.46	0.1	0.5
Critical region: $0.86 \leq iFR \leq 0.93$, $N = 19$									
AS_i	0.56 (0.06)	0.04 (0.01)	0.36 (0.06)	0.95 (0.01)	0.03 (0.01)	0.01 (0.01)	0.5 (0.06)	0.07 (0.02)	0.37 (0.05)
$AS_{T,i}$	0.6 (0.06)	0.04 (0.01)	0.4 (0.06)	0.97 (0.01)	0.04 (0.01)	0.01 (0.01)	0.55 (0.05)	0.09 (0.02)	0.42 (0.05)
WS_i	0.53	0.03	0.39	0.94	0.04	0.01	0.47	0.08	0.39
$WS_{T,i}$	0.58	0.04	0.43	0.96	0.05	0.01	0.52	0.1	0.44

Note: Indices are reported when all 81 measurements are considered, and for cases ($N = 19$) where iFR was in the critical region between 0.86 and 0.93. Results are reported as mean (standard deviation).

[40, 47]. Along with the results depicted in Figure 5, they show that our solver is able to satisfactorily reproduce both unsteady and steady-state haemodynamic indices obtained through 3D simulations, in the case of identical boundary conditions. This choice of boundary conditions, in particular, allowed us to comprehensively assess the correctness of the proposed distributed stenosis model, proving that the steady-state assumption under which it was derived has no significantly negative impact on simulation results. For both scenarios 1 and 2, the observed biases, computed as the difference between the 3D and the 1D-0D estimates, were indeed below 1%. Moreover, Pearson correlation coefficients of 0.98 and 0.97, respectively, indicate a very strong positive correlation between 3D and 1D-0D results. Furthermore, through our solver we were able to correctly match the diagnostic outcome of 96.61% of 3D steady-state estimates and of 97.67% of 3D unsteady estimates.

Since results obtained through our 1D-0D model are comparable to those obtained via 3D simulations, it is possible to employ this computationally cheaper and generally more robust method [41] to explore the parameter space through global sensitivity analysis, which requires a high number of model evaluations, and to assess a large number of modelling assumptions to develop modelling setups that result in reduced uncertainty.

4.2 | Validation of the 1D-0D Model Versus Invasive Measurements

As expected from previously published analyses [25, 41], the mismatch between 1D-0D iFR estimates and invasive measurements is significant, and is likely exacerbated by suboptimal parameter choices: when considering all available measurement locations, the obtained bias is −0.036 with a standard deviation of 0.101, which implies that average 1D iFR predictions consistently overestimate invasive iFR measurements, underestimating stenosis severity.

The diagnostic accuracy, sensitivity, specificity, positive predicted value and negative predicted value for our iFR prediction framework are, respectively, 83.95%, 60%, 91.8%, 70.59% and 87.5%. With the exception of sensitivity and specificity, these results are comparable to the diagnostic efficacy of FFR_{CT} reported in previous multicentre studies [99–101], which reported diagnostic accuracies between 73% and 81%, sensitivities between 86% and 90%, specificities between 54% and 82% and positive and negative predictive values between 65% and 74% and 84% and 93%, respectively. Furthermore, 1D-0D iFR diagnostic accuracy is comparable to that of CCTA scans (79.03% [34]) and to values obtained with an open 3D-0D model by Ma et al. [36] and through deep-learning and CFD-based models by Zhang et al. [35] (respectively 78.72% and 78%). The specificity of our 1D-0D estimates is higher than values reported for FFR_{CT} and in works by Ma et al. [36] and Zhang et al. [35] and comparable with that obtained by Liu et al. [34] through a closed-loop 3D-0D model (92.45%). Sensitivity is, instead, particularly low when compared to values reported for FFR_{CT} [99–101] and for computational iFR by Liu et al. [34], Ma et al. [36] and Zhang et al. [35] (respectively 77.78%, 70.59% and 73%). These differences might be related to parameter choices: Figure 8 highlights how computational iFR predictions are affected by different sources of uncertainty. Looking at the third plot, we can observe that uncertainties in radius, compliance and baseline flow result in very large 95% confidence intervals for lesions with invasively measured iFR below the critical threshold of 0.89. Results obtained through sensitivity analysis and reported in Table 5 identify flow and segmented radius as the two most influential parameters for computational iFR estimation. In particular, our distribution for total coronary flow was obtained assuming a resting baseline state, motivated by the fact that iFR measurements are performed without medications that vasodilate the coronary microcirculation, such as adenosine. The patients were however given other medications such as nitroglycerin and potentially also beta-blockers, which could perturb the flow from normal resting levels. The relatively large bias and general underestimation of stenosis severity by predicted iFR indicate that the modelling pipeline could be improved by better estimation of total coronary flow.

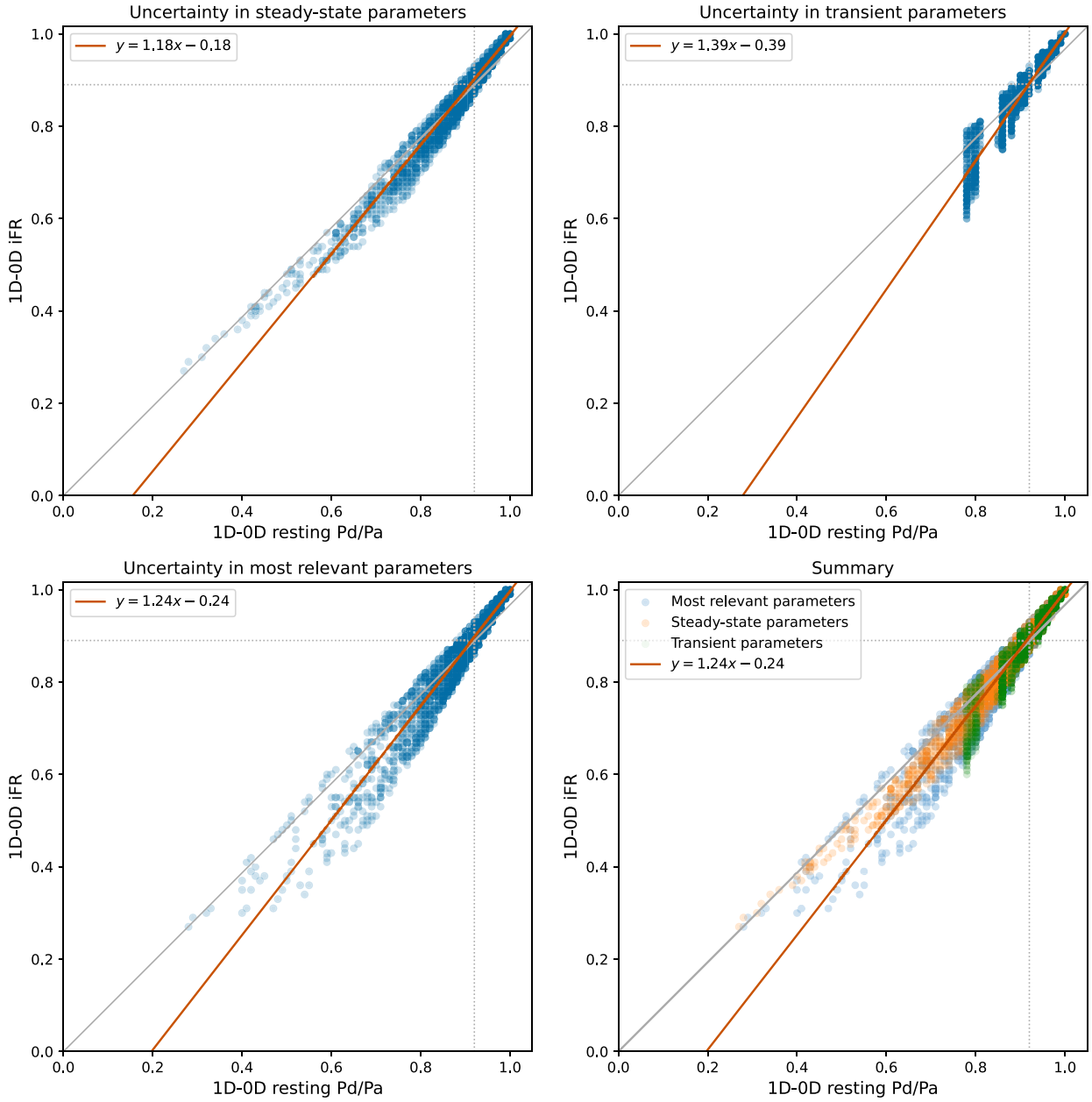

FIGURE 7 | Scatter plots of 1D-0D resting P_d / P_a versus 1D-0D iFR with corresponding coefficients for linear fitting. The plot on the top left was obtained considering all simulations performed accounting for uncertainties in steady-state parameters, that on the top right collects simulation results obtained varying transient parameters and that on the bottom left was obtained considering all simulations performed for the final sensitivity analysis. The plot on the bottom right collects a summary of results obtained through simulations performed for all the three analyses.

TABLE 6 | Comparison of corrected resting P_d / P_a and iFR estimates.

Comparison type	Bias	Acc.	Sens.	Spec.	PPV	NPV
Resting P_d / P_a versus iFR	—	96.77	97.38	96.6	88.19	99.3
Corrected resting P_d / P_a versus iFR	0. (0.018)	96.81	91.33	98.23	93.08	97.75

Note: Diagnostic indices were computed using 0.92 as the critical threshold for resting P_d / P_a and 0.89 as the critical threshold for iFR [40, 47]. When considering the corrected resting P_d / P_a, we employed a threshold of 0.89 for both indices. Results are reported as mean (standard deviation).

4.3 | Sensitivity Analysis

We characterised the uncertainty in iFR predictions based on the inputs associated with inlet and outlet boundary conditions (q_{branch} and $P_{\text{in}}(t)$) and based on parameters that effect the vessel geometry (Δr) and deformation (C_{branch}). The uncertainties in q_{branch} and $P_{\text{in}}(t)$ were estimated based on clinically derived quantities, while Δr and C_{branch} were estimated

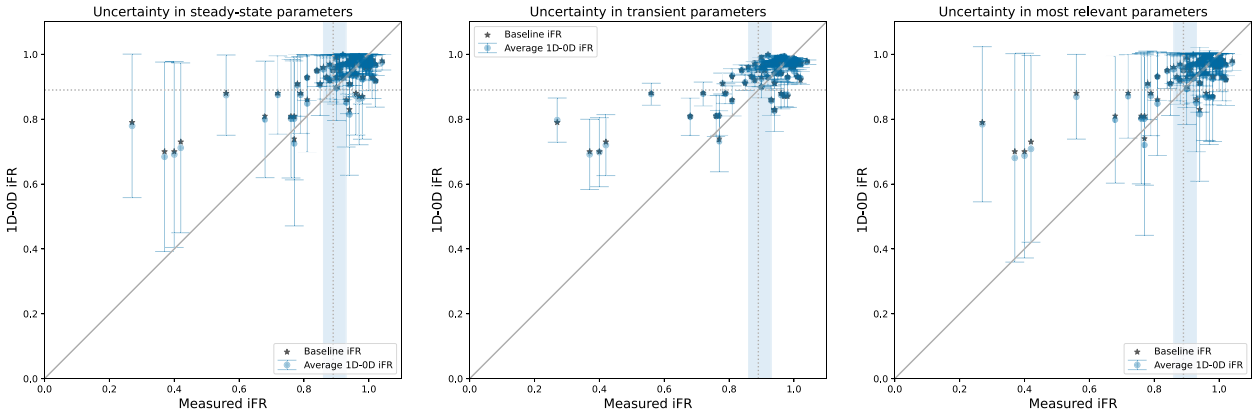

FIGURE 8 | Scatter plots of average 1D-0D iFR estimates obtained through the three sensitivity analyses vs. measured iFR. Blue vertical lines denote two standard deviations (95% confidence interval), and shaded regions identify the critical region between 0.86 and 0.93. Stars denote iFR estimates obtained using baseline patient-specific parameters.

based on the typical image resolution and reported literature variations.

4.3.1 | Sensitivity to Segmented Radius and Baseline Coronary Flow

Consistently with the analysis performed by Fossan et al. [41] concerning computational FFR estimation, uncertainties about vessel segmentation, represented here by Δr, and flow to the considered coronary branch, described by the multiplier Δq_{branch}, have the highest impact on iFR predictions when assessing parameters that impact the steady-state portion of the pipeline presented in Section 2.3. Moreover, comparable sensitivity indices were obtained in the overall final analysis. Dissimilarly to the considerations made concerning the impact of uncertainties in vessel radius on steady-state FFR predictions, there is no significant difference between averaged and weighted sensitivity indices and, as we can see in Table 5, the influence of Δr is comparable when considering the entire set of lesions and lesions within the critical iFR range between 0.86 and 0.93 [47]. This indicates that accurate segmentations are fundamental to obtain accurate iFR estimates, independently of stenosis severity, and suggests that cardiac-cycle averaged indices obtained through steady-state simulations might better classify borderline cases.

The chosen coronary flow was split among network outlets to define the outlet boundary conditions employed for the steady-state portion of the pipeline. Through this step, we estimated resistances employed to parametrise 0D models coupled to terminal 1D vessels, which in turn are major determinants of diastolic pressure decay. The results show that the impact of coronary arterial flow is comparable to that of segmented radius and is slightly higher when considering weighted sensitivity indices compared to averaged ones. Consequently, it is crucial to correctly model flow through the coronary tree to obtain reliable iFR estimates. To this end, methods to directly measure total baseline coronary flow are being developed in the context of ultrasound imaging and magnetic resonance imaging [102, 103]. Nonetheless, to our knowledge, such methods have not been used yet in the context of model-based iFR or FFR predictions [33].

4.3.2 | Sensitivity to Pressure-Related Parameters

Previously published analyses [33, 41, 43] reported that prescribed inlet pressure has a very low impact on steady-state FFR prediction frameworks. Since the fifth step of the proposed 1D-0D pipeline for computational iFR prediction (see Section 2.3) consists of a transient simulation performed prescribing a time-dependent aortic pressure waveform at the inlet of the network, we chose to consider uncertainties in pressure-related parameters to assess whether modifying its shape has an impact on iFR estimates related to variations in diastolic pressure decay. The obtained averaged and weighted sensitivity indices confirm that the impact of this quantity is negligible also when considering a transient iFR prediction framework. This suggests that a standard population-based pressure waveform could be used for simulations, without requiring a patient-specific parametrisation.

4.3.3 | Sensitivity to Coronary Arterial Compliance

Coronary arterial compliance has a relatively high impact on iFR predictions with respect to other parameters employed for the unsteady portion of the pipeline, since it is involved in the parametrisation of Mantero lumped parameter models. Nonetheless, its overall impact on iFR prediction is low compared to steady-state parameters Δr and Δq_{branch}, suggesting that iFR estimation is mostly influenced by steady-state quantities. This consideration motivates the comparison reported in Figure 7 between computational estimates of resting P_d/P_a and iFR. The correlation between the two indices is satisfactory and is maintained when introducing uncertainties related to the unsteady portion of the pipeline. Moreover, while scatter is present, it is very low around the critical threshold (0.89 for iFR, 0.92 for resting P_d/P_a [40, 47]), suggesting that the ability of the two indices of discriminating functionally significant lesions is comparable. This is confirmed by numerical results reported in Table 6, which highlight also the equivalence between resting P_d/P_a with a threshold of 0.92 and the corrected resting P_d/P_a value obtained through the linear relationship (47) with a threshold of 0.89. This indicates that unsteady simulations could reasonably be replaced with steady-state ones applying an appropriate correction coefficient.

4.4 | Limitations

The present work has several limitations. First, when parametrising the lumped parameter models prescribed at terminal vessels, we assumed that all intramyocardial vessels are subject to left ventricular pressure. This was motivated by the consideration that the only microvasculature that is subjected purely to right ventricular pressure originates from vessels perfusing the free wall of the right ventricle, which corresponds to only about 20% of the total myocardial volume. However, in future work we plan to address this potential issue by integrating the coronary geometries obtained through segmentation within a cardiac perfusion map, so that we can parametrise the terminal lumped parameter models in terms of left ventricular, right ventricular and septal pressures depending on the perfused region. Secondly, our 1D-0D model is not perfectly reproducing 3D results. This is partly due to the fact that we derived our stenosis model under the assumption of steady flow in the 1D blood flow equations, and assuming that inertial contributions to the pressure drop are negligible. This choice was performed due to the significant advantages for the numerical treatment of the problem, consistently with the approach by Jin and Alastruey [59] and by Steele et al. [58]. Additionally, it might also be related to our choice of modelling pressure drops across lesions using as basis the work by Young et al. [60], which has limited validity in stenoses with non-cylindrical shape and abrupt changes in radius, and of neglecting the space–time dependence of obtained coefficients. Future work will be devoted to exploring the impact on iFR estimates of choosing different 0D stenosis models as the basis for our distributed approach, such as the machine-learning augmented 0D stenosis model proposed by Fossan et al. [25], or the stenosis models by Itu et al. [104] and Huo et al. [105]. Another possible approach would be that proposed by Bessems et al. [106]. In addition, we plan to employ a space–time dependent viscous loss coefficient $R_v(x,t)$, where we include the dependence of stenotic areas A_s and diameters D_s on both space and time. Further limitations are related to the parameters we chose for UQ&SA. Similarly to what was done in Fossan et al. [41] and Müller et al. [33], we modelled the uncertainty in geometry through a global parameter affecting the entire coronary branch, which may result in an increased influence of this parameter. Moreover, we assessed only the impact that baseline coronary flow has on iFR estimation, without including uncertainties related to its distribution among network outlets.

5 | Conclusions and Future Work

In this work, we proposed and validated a 1D-0D model for iFR prediction with distributed stenosis model, and tested the impact of uncertainties in geometry, flow, compliance and pressure-related parameters through UQ&SA techniques. Validation was performed both in terms of resting P_d/P_a versus steady-state 3D predictions on a set of 679 stenoses, and in terms of iFR with respect to 43 unsteady 3D estimates and of 81 invasive measurements, pertaining to 52 patients with stable CAD. UQ&SA was performed only for the 81 lesions for which invasive measurements were available.

Validation confirmed that the proposed 1D-0D model introduces very small errors with respect to both the steady-state and unsteady 3D model when assessing haemodynamic indices of interest. This implies that 1D-0D models can be employed for the exploration of modelling simplifying assumptions and of the parameter space, to develop modelling setups that are characterised by reduced uncertainty.

Through UQ&SA, we have shown that iFR estimation is mostly affected by uncertainties in parameters related to the steady-state portion of the pipeline, and, in particular, by vascular geometry and baseline flow entering the considered coronary branch. Furthermore, the large bias observed comparing 1D-0D iFR estimates to invasive iFR measurements indicates that the modelling pipeline could be improved through a more accurate estimation of total coronary flow.

The good correlation observed between predictions of resting P_d/P_a and predicted iFR, which is maintained when introducing uncertainties related to the unsteady portion of the pipeline, suggests that unsteady simulations for iFR can be replaced by steady-state ones introducing an appropriate correction factor, without compromising the diagnostic quality of the obtained index. On the one hand, future work will address limitations highlighted above, and on the other hand, will be targeted towards optimisation of the modelling pipeline for iFR prediction.

Acknowledgements

C. Dalmaso and L.O. Müller acknowledge the financial support of the GNCS group of INdAM. Computational resources in Norwegian HPC infrastructure were granted by the Norwegian Research Council by Project Nr. NN9713K.

Ethics Statement

All procedures performed in studies involving human participants were in accordance with the ethical standards of the institutional and/or national research committee and with the 1964 Helsinki declaration and its later amendments or comparable ethical standards.

Conflicts of Interest

The authors declare no conflicts of interest.

Data Availability Statement

The data and codes that support the findings of this study are available on request from the corresponding author. The data are not publicly available due to privacy or ethical restrictions.

References

1. A. Timmis, P. Vardas, N. Townsend, et al., "European Society of Cardiology: Cardiovascular Disease Statistics 2021," *European Heart Journal* 43, no. 8 (2022): 716–799, https://doi.org/10.1093/eurheartj/ehab892.

2. C. W. Tsao, A. W. Aday, Z. I. Almarzooq, et al., "Heart Disease and Stroke Statistics—2023 Update: A Report From the American Heart Association," *Circulation* 147, no. 8 (2023): e93–e621, https://doi.org/10.1161/CIR.0000000000001123.

3. J. Knuuti, W. Wijns, A. Saraste, et al., "2019 ESC Guidelines for the Diagnosis and Management of Chronic Coronary Syndromes: The Task Force for the Diagnosis and Management of Chronic Coronary

Syndromes of the European Society of Cardiology (ESC)," *European Heart Journal* 41, no. 3 (2019): 407–477, https://doi.org/10.1093/eurheartj/ehz425.

4. S. H. Investigators, "CT Coronary Angiography in Patients With Suspected Angina due to Coronary Heart Disease (SCOT-HEART): An Open-Label, Parallel-Group, Multicentre Trial," *Lancet* 385, no. 9985 (2015): 2383–2391, https://doi.org/10.1016/S0140-6736(15)60291-4.

5. P. S. Douglas, U. Hoffmann, M. R. Patel, et al., "Outcomes of Anatomical Versus Functional Testing for Coronary Artery Disease," *New England Journal of Medicine* 372, no. 14 (2015): 1291–1300, https://doi.org/10.1056/NEJMoa1415516.

6. H. J. Chang, F. Y. Lin, D. Gebow, et al., "Selective Referral Using CCTA Versus Direct Referral for Individuals Referred to Invasive Coronary Angiography for Suspected CAD: A Randomized, Controlled, Open-Label Trial," *JACC: Cardiovascular Imaging* 12, no. 7 Part 2 (2019): 1303–1312, https://doi.org/10.1016/j.jcmg.2018.09.018.

7. L. J. Shaw, J. Hausleiter, S. Achenbach, et al., "Coronary Computed Tomographic Angiography as a Gatekeeper to Invasive Diagnostic and Surgical Procedures: Results From the Multicenter CONFIRM (Coronary CT Angiography Evaluation for Clinical Outcomes: An International Multicenter) Registry," *Journal of the American College of Cardiology* 60, no. 20 (2012): 2103–2114, https://doi.org/10.1093/eurheartj/ehv444.

8. N. H. Pijls, v P. Schaardenburgh, G. Manoharan, et al., "Percutaneous Coronary Intervention of Functionally Nonsignificant Stenosis: 5-Year Follow-Up of the DEFER Study," *Journal of the American College of Cardiology* 49, no. 21 (2007): 2105–2111, https://doi.org/10.1016/j.jacc.2007.01.087.

9. N. H. Pijls, W. F. Fearon, P. A. Tonino, et al., "Fractional Flow Reserve Versus Angiography for Guiding Percutaneous Coronary Intervention in Patients With Multivessel Coronary Artery Disease: 2-Year Follow-Up of the FAME (Fractional Flow Reserve Versus Angiography for Multivessel Evaluation) Study," *Journal of the American College of Cardiology* 56, no. 3 (2010): 177–184, https://doi.org/10.1016/j.jacc.2010.04.012.

10. I. Y. Elgendy, C. R. Conti, and A. A. Bavry, "Fractional Flow Reserve: An Updated Review," *Clinical Cardiology* 37, no. 6 (2014): 371–380, https://doi.org/10.1002/clc.22273.

11. S. Sen, J. Escaned, I. S. Malik, et al., "Development and Validation of a New Adenosine-Independent Index of Stenosis Severity From Coronary Wave–Intensity Analysis: Results of the ADVISE (ADenosine Vasodilator Independent Stenosis Evaluation) Study," *Journal of the American College of Cardiology* 59, no. 15 (2012): 1392–1402, https://doi.org/10.1016/j.jacc.2011.11.003.

12. S. Sen, K. N. Asrress, S. Nijjer, et al., "Diagnostic Classification of the Instantaneous Wave-Free Ratio Is Equivalent to Fractional Flow Reserve and Is Not Improved With Adenosine Administration: Results of CLARIFY (Classification Accuracy of Pressure-Only Ratios Against Indices Using Flow Study)," *Journal of the American College of Cardiology* 61, no. 13 (2013): 1409–1420, https://doi.org/10.1016/j.jacc.2013.01.034.

13. M. Götberg, C. M. Cook, S. Sen, S. Nijjer, J. Escaned, and J. E. Davies, "The Evolving Future of Instantaneous Wave-Free Ratio and Fractional Flow Reserve," *Journal of the American College of Cardiology* 70, no. 11 (2017): 1379–1402, https://doi.org/10.1016/j.jacc.2017.07.770.

14. J. Knuuti and A. Saraste, "ESC 2019 Guidelines for the Diagnosis and Management of Chronic Coronary Syndromes," *Herz* 45, no. 5 (2020): 409–420, https://doi.org/10.1007/s00059-020-04935-x.

15. A. Rossi, S. L. Papadopoulou, F. Pugliese, et al., "Quantitative Computed Tomographic Coronary Angiography: Does It Predict Functionally Significant Coronary Stenoses?," *Circulation: Cardiovascular Imaging* 7, no. 1 (2014): 43–51, https://doi.org/10.1161/CIRCIMAGING.112.000277.

16. J. E. Davies, S. Sen, H. M. Dehbi, et al., "Use of the Instantaneous Wave-Free Ratio or Fractional Flow Reserve in PCI," *New England Journal of Medicine* 376, no. 19 (2017): 1824–1834, https://doi.org/10.1056/NEJMoa1700445.

17. M. Götberg, E. H. Christiansen, I. J. Gudmundsdottir, et al., "Instantaneous Wave-Free Ratio Versus Fractional Flow Reserve to Guide PCI," *New England Journal of Medicine* 376, no. 19 (2017): 1813–1823, https://doi.org/10.1056/NEJMoa1616540.

18. S. Baumann, L. Chandra, E. Skarga, et al., "Instantaneous Wave-Free Ratio (iFR®) to Determine Hemodynamically Significant Coronary Stenosis: A Comprehensive Review," *World Journal of Cardiology* 10, no. 12 (2018): 267–277, https://doi.org/10.4330/wjc.v10.i12.267.

19. S. De Rosa, A. Polimeni, R. Petraco, J. E. Davies, and C. Indolfi, "Diagnostic Performance of the Instantaneous Wave-Free Ratio: Comparison With Fractional Flow Reserve," *Circulation: Cardiovascular Interventions* 11, no. 1 (2018): e004613, https://doi.org/10.1161/CIRCINTERVENTIONS.116.004613.

20. C. M. Cook, R. Petraco, M. J. Shun-Shin, et al., "Diagnostic Accuracy of Computed Tomography–Derived Fractional Flow Reserve: A Systematic Review," *JAMA Cardiology* 2, no. 7 (2017): 803–810, https://doi.org/10.1001/jamacardio.2017.1314.

21. M. Kruk, Ł. Wardziak, M. Demkow, et al., "Workstation-Based Calculation of CTA-Based FFR for Intermediate Stenosis," *JACC: Cardiovascular Imaging* 9, no. 6 (2016): 690–699, https://doi.org/10.1016/j.jcmg.2015.09.019.

22. B. S. Ko, J. D. Cameron, R. K. Munnur, et al., "Noninvasive CT-Derived FFR Based on Structural and Fluid Analysis: A Comparison With Invasive FFR for Detection of Functionally Significant Stenosis," *JACC: Cardiovascular Imaging* 10, no. 6 (2017): 663–673, https://doi.org/10.1016/j.jcmg.2016.07.005.

23. P. M. Donnelly, M. Kolossváry, J. Karády, et al., "Experience With an On-Site Coronary Computed Tomography-Derived Fractional Flow Reserve Algorithm for the Assessment of Intermediate Coronary Stenoses," *American Journal of Cardiology* 121, no. 1 (2018): 9–13, https://doi.org/10.1016/j.amjcard.2017.09.018.

24. P. J. Blanco, C. A. Bulant, L. O. Müller, et al., "Comparison of 1D and 3D Models for the Estimation of Fractional Flow Reserve," *Scientific Reports* 8, no. 1 (2018): 1–12, https://doi.org/10.1038/s41598-018-35344-0.

25. F. E. Fossan, L. O. Müller, J. Sturdy, et al., "Machine Learning Augmented Reduced-Order Models for FFR-Prediction," *Computer Methods in Applied Mechanics and Engineering* 384 (2021): 113892, https://doi.org/10.1016/j.cma.2021.113892.

26. J. M. Carson, S. Pant, C. Roobottom, et al., "Non-Invasive Coronary CT Angiography-Derived Fractional Flow Reserve: A Benchmark Study Comparing the Diagnostic Performance of Four Different Computational Methodologies," *International Journal for Numerical Methods in Biomedical Engineering* 35, no. 10 (2019): e3235, https://doi.org/10.1002/cnm.3235.

27. C. Bulant, P. Blanco, G. M. Talou, C. G. Bezerra, P. Lemos, and R. Feijóo, "A Head-To-Head Comparison Between CT-and IVUS-Derived Coronary Blood Flow Models," *Journal of Biomechanics* 51 (2017): 65–76, https://doi.org/10.1016/j.jbiomech.2016.11.070.

28. J. K. Min, J. Leipsic, M. J. Pencina, et al., "Diagnostic Accuracy of Fractional Flow Reserve From Anatomic CT Angiography," *Journal of the American Medical Association* 308, no. 12 (2012): 1237–1245, https://doi.org/10.1001/2012.jama.11274.

29. P. D. Morris, D. Ryan, A. C. Morton, et al., "Virtual Fractional Flow Reserve From Coronary Angiography: Modeling the Significance of Coronary Lesions: Results From the VIRTU-1 (VIRTUal Fractional Flow Reserve From Coronary Angiography) Study," *JACC: Cardiovascular Interventions* 6, no. 2 (2013): 149–157, https://doi.org/10.1016/j.jcin.2012.08.024.

30. S. Tu, E. Barbato, Z. Köszegi, et al., "Fractional Flow Reserve Calculation From 3-Dimensional Quantitative Coronary Angiography and TIMI Frame Count: A Fast Computer Model to Quantify the Functional Significance of Moderately Obstructed Coronary Arteries," *JACC: Cardiovascular Interventions* 7, no. 7 (2014): 768–777, https://doi.org/10.1016/j.jcin.2014.03.004.

31. R. C. Gosling, P. D. Morris, D. A. Silva Soto, P. V. Lawford, D. R. Hose, and J. P. Gunn, "Virtual Coronary Intervention: A Treatment Planning Tool Based Upon the Angiogram," *JACC: Cardiovascular Imaging* 12, no. 5 (2019): 865–872, https://doi.org/10.1016/j.jcmg.2018.01.019.

32. C. A. Taylor, T. A. Fonte, and J. K. Min, "Computational Fluid Dynamics Applied to Cardiac Computed Tomography for Noninvasive Quantification of Fractional Flow Reserve: Scientific Basis," *Journal of the American College of Cardiology* 61, no. 22 (2013): 2233–2241, https://doi.org/10.1016/j.jacc.2012.11.083.

33. L. O. Müller, F. E. Fossan, A. T. Bråten, A. Jørgensen, R. Wiseth, and L. R. Hellevik, "Impact of Baseline Coronary Flow and Its Distribution on Fractional Flow Reserve Prediction," *International Journal for Numerical Methods in Biomedical Engineering* 37, no. 11 (2021): e3246, https://doi.org/10.1002/cnm.3246.

34. J. Liu, B. Li, Y. Zhang, et al., "A High-Fidelity Geometric Multiscale Hemodynamic Model for Predicting Myocardial Ischemia," *Computer Methods and Programs in Biomedicine* 233 (2023): 107476, https://doi.org/10.1016/j.cmpb.2023.107476.

35. J. Zhang, K. Xu, Y. Hu, et al., "Diagnostic Performance of Deep Learning and Computational Fluid Dynamics-Based Instantaneous Wave-Free Ratio Derived From Computed Tomography Angiography," *BMC Cardiovascular Disorders* 22, no. 1 (2022): 33, https://doi.org/10.1186/s12872-022-02469-0.

36. Y. Ma, H. Liu, Y. Hou, et al., "Instantaneous Wave-Free Ratio Derived From Coronary Computed Tomography Angiography in Evaluation of Ischemia-Causing Coronary Stenosis: Feasibility and Initial Clinical Research," *Medicine* 96, no. 4 (2017): e5979, https://doi.org/10.1097/MD.0000000000005979.

37. Y. Ma, Y. Hou, A. Qiao, et al., "Non-invasive Instantaneous Wave-Free Ratio Using Coronary CT Angiography: Diagnostic Performance for Evaluation of Ischaemia-Causing Coronary Stenosis Confirmed by Invasive Fractional Flow Reserve," *Clinical Radiology* 73, no. 11 (2018): 983, https://doi.org/10.1016/j.crad.2018.07.098.

38. X. Ge, Y. Liu, Z. Yin, et al., "Comparison of Instantaneous Wave-Free Ratio (iFR) and Fractional Flow Reserve (FFR) With Respect to Their Sensitivities to Cardiovascular Factors: A Computational Model-Based Study," *Journal of Interventional Cardiology* 2020 (2020): 1–12, https://doi.org/10.1155/2020/4094121.

39. J. M. Carson, C. Roobottom, R. Alcock, and P. Nithiarasu, "Computational Instantaneous Wave-Free Ratio (IFR) for Patient-Specific Coronary Artery Stenoses Using 1D Network Models," *International Journal for Numerical Methods in Biomedical Engineering* 35, no. 11 (2019): e3255, https://doi.org/10.1002/cnm.3255.

40. d G A. Waard, I. Danad, R. Petraco, et al., "Fractional Flow Reserve, Instantaneous Wave-Free Ratio, and Resting pd/pa Compared With [15O] H_2O Positron Emission Tomography Myocardial Perfusion Imaging: A PACIFIC Trial Sub-Study," *European Heart Journal* 39, no. 46 (2018): 4072–4081, https://doi.org/10.1093/eurheartj/ehy632.

41. F. E. Fossan, J. Sturdy, L. O. Müller, et al., "Uncertainty Quantification and Sensitivity Analysis for Computational FFR Estimation in Stable Coronary Artery Disease," *Cardiovascular Engineering and Technology* 9, no. 4 (2018): 597–622, https://doi.org/10.1007/s13239-018-00388-w.

42. X. Ge, Z. Yin, Y. Fan, Y. Vassilevski, and F. Liang, "A Multi-Scale Model of the Coronary Circulation Applied to Investigate Transmural Myocardial Flow," *International Journal for Numerical Methods in Biomedical Engineering* 34, no. 10 (2018): e3123, https://doi.org/10.1002/cnm.3123.

43. P. D. Morris, D. A. Silva Soto, J. F. Feher, et al., "Fast Virtual Fractional Flow Reserve Based Upon Steady-State Computational Fluid Dynamics Analysis: Results From the VIRTU-Fast Study," *Basic to Translational Science* 2, no. 4 (2017): 434–446, https://doi.org/10.1016/j.jacbts.2017.04.003.

44. S. Sankaran, H. J. Kim, G. Choi, and C. A. Taylor, "Uncertainty Quantification in Coronary Blood Flow Simulations: Impact of Geometry, Boundary Conditions and Blood Viscosity," *Journal of Biomechanics* 49, no. 12 (2016): 2540–2547, https://doi.org/10.1016/j.jbiomech.2016.01.002.

45. V. G. Eck, W. P. Donders, J. Sturdy, et al., "A Guide to Uncertainty Quantification and Sensitivity Analysis for Cardiovascular Applications," *International Journal for Numerical Methods in Biomedical Engineering* 32, no. 8 (2016): e02755, https://doi.org/10.1002/cnm.2755.

46. A. Bråten and R. Wiseth, "Diagnostic Accuracy of CT-FFR Compared to Invasive Coronar Angiography With Fractional Flow Reserve-Full Text View-Clinicaltrials," 2017, https://clinicaltrials. gov/ct2/show/NCT03045601.

47. R. Petraco, J. Escaned, S. Sen, et al., "Classification Performance of Instantaneous Wave-Free Ratio (iFR) and Fractional Flow Reserve in a Clinical Population of Intermediate Coronary Stenoses: Results of the ADVISE Registry," *EuroIntervention: Journal OF EuroPCR in Collaboration with the Working Group on Interventional Cardiology of the European Society of Cardiology* 9, no. 1 (2013): 91–101, https://doi.org/10.1016/10.4244/EIJV9I1A14.

48. S. Gaur, K. A. Øvrehus, D. Dey, et al., "Coronary Plaque Quantification and Fractional Flow Reserve by Coronary Computed Tomography Angiography Identify Ischaemia-Causing Lesions," *European Heart Journal* 37, no. 15 (2016): 1220–1227, https://doi.org/10.1093/eurheartj/ehv690.

49. L. Antiga, M. Piccinelli, L. Botti, B. Ene-Iordache, A. Remuzzi, and D. A. Steinman, "An Image-Based Modeling Framework for Patient-Specific Computational Hemodynamics," *Medical & Biological Engineering & Computing* 46 (2008): 1097–1112, https://doi.org/10.1007/s11517-008-0420-1.

50. L. Formaggia, A. Quarteroni, and A. Veneziani, *Cardiovascular Mathematics: Modeling and Simulation of the Circulatory System 1* (Milan, Italy: Springer-Verlag, 2010), https://doi.org/10.1007/978-88-470-1152-6.

51. T. J. Hughes and J. Lubliner, "On the One-Dimensional Theory of Blood Flow in the Larger Vessels," *Mathematical Biosciences* 18, no. 1–2 (1973): 161–170, https://doi.org/10.1016/0025-5564(73)90027-8.

52. T. J. Hughes, *A Study of the One-Dimensional Theory of Arterial Pulse Propagation* (Structural Engineering Laboratory: University of California, 1974).

53. E. F. Toro and A. Siviglia, "Flow in Collapsible Tubes With Discontinuous Mechanical Properties: Mathematical Model and Exact Solutions," *Communications in Computational Physics* 13, no. 2 (2013): 361–385, https://doi.org/10.4208/cicp.210611.240212a.

54. A. Spilimbergo, E. F. Toro, and L. O. Müller, "One-Dimensional Blood Flow With Discontinuous Properties and Transport: Mathematical Analysis and Numerical Schemes," *Communications in Computational Physics* 29, no. 3 (2021): 649–697, https://doi.org/10.4208/cicp.OA-2020-0132.

55. J. P. Mynard and J. J. Smolich, "One-Dimensional Haemodynamic Modeling and Wave Dynamics in the Entire Adult Circulation," *Annals of Biomedical Engineering* 43, no. 6 (2015): 1443–1460, https://doi.org/10.1007/s10439-015-1313-8.

56. L. O. Müller and E. F. Toro, "Well-Balanced High-Order Solver for Blood Flow in Networks of Vessels With Variable Properties," *International Journal for Numerical Methods in Biomedical Engineering* 29, no. 12 (2013): 1388–1411, https://doi.org/10.1002/cnm.2580.

57. L. O. Müller, P. J. Blanco, S. M. Watanabe, and R. A. Feijóo, "A High-Order Local Time Stepping Finite Volume Solver for One-Dimensional Blood Flow Simulations: Application to the ADAN Model," *International Journal for Numerical Methods in Biomedical Engineering* 32, no. 10 (2016): e02761, https://doi.org/10.1002/cnm.2761.

58. B. N. Steele, J. Wan, J. P. Ku, T. J. Hughes, and C. A. Taylor, "In Vivo Validation of a One-Dimensional Finite-Element Method for Predicting Blood Flow in Cardiovascular Bypass Grafts," *IEEE Transactions on Biomedical Engineering* 50, no. 6 (2003): 649–656, https://doi.org/10.1109/TBME.2003.812201.

59. W. Jin and J. Alastruey, "Arterial Pulse Wave Propagation Across Stenoses and Aneurysms: Assessment of One-Dimensional Simulations Against Three-Dimensional Simulations and In Vitro Measurements," *Journal of the Royal Society Interface* 18, no. 177 (2021): 20200881, https://doi.org/10.1098/rsif.2020.0881.

60. D. F. Young and F. Y. Tsai, "Flow Characteristics in Models of Arterial Stenoses—II. Unsteady Flow," *Journal of Biomechanics* 6, no. 5 (1973): 547–559.

61. F. Liang, K. Fukasaku, H. Liu, and S. Takagi, "A Computational Model Study of the Influence of the Anatomy of the Circle of Willis on Cerebral Hyperperfusion Following Carotid Artery Surgery," *Biomedical Engineering Online* 10, no. 1 (2011): 1–22, https://doi.org/10.1186/1475-925X-10-84.

62. B. D. Seeley and D. F. Young, "Effect of Geometry on Pressure Losses Across Models of Arterial Stenoses," *Journal of Biomechanics* 9, no. 7 (1976): 439–448, https://doi.org/10.1016/0021-9290(76)90086-5.

63. S. Mantero, R. Pietrabissa, and R. Fumero, "The Coronary Bed and Its Role in the Cardiovascular System: A Review and an Introductory Single-Branch Model," *Journal of Biomedical Engineering* 14, no. 2 (1992): 109–116, https://doi.org/10.1016/0141-5425(92)90015-D.

64. B. Ghitti, P. J. Blanco, E. F. Toro, and L. O. Müller, "Construction of Hybrid 1D-0D Networks for Efficient and Accurate Blood Flow Simulations," *International Journal for Numerical Methods in Fluids* 95, no. 2 (2023): 262–312, https://doi.org/10.1002/fld.5149.

65. d G. Simone, M. J. Roman, M. J. Koren, G. A. Mensah, A. Ganau, and R. B. Devereux, "Stroke Volume/Pulse Pressure Ratio and Cardiovascular Risk in Arterial Hypertension," *Hypertension* 33, no. 3 (1999): 800–805, https://doi.org/10.1161/01.HYP.33.3.800.

66. S. Sakamoto, S. Takahashi, A. U. Coskun, et al., "Relation of Distribution of Coronary Blood Flow Volume to Coronary Artery Dominance," *American Journal of Cardiology* 111, no. 10 (2013): 1420–1424, https://doi.org/10.1016/j.amjcard.2013.01.290.

67. Y. Huo and G. S. Kassab, "Intraspecific Scaling Laws of Vascular Trees," *Journal of the Royal Society Interface* 9, no. 66 (2012): 190–200, https://doi.org/10.1098/rsif.2011.0270.

68. B. A. Haluska, L. Jeffriess, R. Fathi, P. M. Mottram, S. G. Carlier, and T. H. Marwick, "Pulse Pressure versus Total Arterial Compliance as a Marker of Arterial Health," *European Journal of Clinical Investigation* 35, no. 7 (2005): 438–443, https://doi.org/10.1111/j.1365-2362.2005.01513.x.

69. C. D. Murray, "The Physiological Principle of Minimum Work: I. The Vascular System and the Cost of Blood Volume," *Proceedings of the National Academy of Sciences* 12, no. 3 (1926): 207–214, https://doi.org/10.1073/pnas.12.3.207.

70. K. H. Choi, J. Park, J. M. Lee, et al., "Comparison of Current and Novel ECG-Independent Algorithms for Resting Pressure Derived Physiologic Indices," *IEEE Access* 7 (2019): 144313–144323, https://doi.org/10.1109/ACCESS.2019.2940085.

71. C. Parés, "Numerical Methods for Nonconservative Hyperbolic Systems: A Theoretical Framework," *SIAM Journal on Numerical Analysis* 44, no. 1 (2006): 300–321, https://doi.org/10.1137/050628052.

72. J. Alastruey, K. Parker, and S. J. Sherwin, "Arterial Pulse Wave Haemodynamics," in *11th International Conference on Pressure Surges* (Portugal: Virtual PiE Led t/a BHR Group Lisbon, 2012), 401–443.

73. J. P. Mynard and P. Nithiarasu, "A 1D Arterial Blood Flow Model Incorporating Ventricular Pressure, Aortic Valve and Regional Coronary Flow Using the Locally Conservative Galerkin (LCG) Method," *Communications in Numerical Methods in Engineering* 24, no. 5 (2008): 367–417, https://doi.org/10.1002/cnm.1117.

74. S. M. Watanabe, P. J. Blanco, and R. A. Feijóo, "Mathematical Model of Blood Flow in an Anatomically Detailed Arterial Network of the Arm," *ESAIM. Mathematical Modelling and Numerical Analysis* 47, no. 4 (2013): 961–985, https://doi.org/10.1051/m2an/2012053.

75. N. Cavallini, V. Caleffi, and V. Coscia, "Finite Volume and WENO Scheme in One-Dimensional Vascular System Modelling," *Computers & Mathematics with Applications* 56, no. 9 (2008): 2382–2397, https://doi.org/10.1016/j.camwa.2008.05.039.

76. D. Elad, D. Katz, E. Kimmel, and S. Einav, "Numerical Schemes for Unsteady Fluid Flow Through Collapsible Tubes," *Journal of Biomedical Engineering* 13, no. 1 (1991): 10–18.

77. M. S. Olufsen, C. S. Peskin, W. Y. Kim, E. M. Pedersen, A. Nadim, and J. Larsen, "Numerical Simulation and Experimental Validation of Blood Flow in Arteries With Structured-Tree Outflow Conditions," *Annals of Biomedical Engineering* 28 (2000): 1281–1299, https://doi.org/10.1114/1.1326031.

78. E. Boileau, P. Nithiarasu, P. J. Blanco, et al., "A Benchmark Study of Numerical Schemes for One-Dimensional Arterial Blood Flow Modelling," *International Journal for Numerical Methods in Biomedical Engineering* 31, no. 10 (2015): e02732, https://doi.org/10.1002/cnm.2732.

79. X. Wang, J. M. Fullana, and P. Y. Lagrée, "Verification and Comparison of Four Numerical Schemes for a 1D Viscoelastic Blood Flow Model," *Computer Methods in Biomechanics and Biomedical Engineering* 18, no. 15 (2015): 1704–1725.

80. W. Kroon, W. Huberts, M. Bosboom, and F. Van De Vosse, "A Numerical Method of Reduced Complexity for Simulating Vascular Hemodynamics Using Coupled 0D Lumped and 1D Wave Propagation Models," *Computational and Mathematical Methods in Medicine* 2012 (2012): 1–10, https://doi.org/10.1155/2012/156094.

81. J. Carson and R. Van Loon, "An Implicit Solver for 1D Arterial Network Models," *International Journal for Numerical Methods in Biomedical Engineering* 33, no. 7 (2017): e2837, https://doi.org/10.1002/cnm.2837.

82. N. C. Nguyen, J. Peraire, and B. Cockburn, "An Implicit High-Order Hybridizable Discontinuous Galerkin Method for the Incompressible Navier–Stokes Equations," *Journal of Computational Physics* 230, no. 4 (2011): 1147–1170, https://doi.org/10.1016/j.jcp.2010.10.032.

83. M. Liu, G. Gao, H. Zhu, and C. Jiang, "A Cell-Based Smoothed Finite Element Method Stabilized by Implicit SUPG/SPGP/Fractional Step Method for Incompressible Flow," *Engineering Analysis with Boundary Elements* 124 (2021): 194–210.

84. F. Setzwein, P. Ess, and P. Gerlinger, "An Implicit High-Order k-Exact Finite-Volume Approach on Vertex-Centered Unstructured Grids for Incompressible Flows," *Journal of Computational Physics* 446 (2021): 110629, https://doi.org/10.1016/j.jcp.2021.110629.

85. A. Lucca, S. Busto, and M. Dumbser, "An Implicit Staggered Hybrid Finite Volume/Finite Element Solver for the Incompressible Navier-Stokes Equations," 2023, arXiv.

86. V. Casulli, M. Dumbser, and E. F. Toro, "Semi-Implicit Numerical Modeling of Axially Symmetric Flows in Compliant Arterial Systems," *International Journal for Numerical Methods in Biomedical Engineering* 28, no. 2 (2012): 257–272, https://doi.org/10.1002/cnm.1464.

87. A. Lucca, S. Busto, L. Müller, E. Toro, and M. Dumbser, "A Semi-Implicit Finite Volume Scheme for Blood Flow in Elastic and Viscoelastic

Vessels," *Journal of Computational Physics* 495 (2023): 112530, https://doi.org/10.1016/j.jcp.2023.112530.

88. E. F. Toro, *Riemann Solvers and Numerical Methods for Fluid Dynamics: A Practical Introduction* (Berlin, Heidelberg: Springer, 2009), https://doi.org/10.1007/b79761.

89. M. J. Castro and C. Parés, "Well-Balanced High-Order Finite Volume Methods for Systems of Balance Laws," *Journal of Scientific Computing* 82, no. 2 (2020): 1–48, https://doi.org/10.1007/s10915-020-01149-5.

90. L. O. Müller, C. Parés, and E. F. Toro, "Well-Balanced High-Order Numerical Schemes for One-Dimensional Blood Flow in Vessels With Varying Mechanical Properties," *Journal of Computational Physics* 242 (2013): 53–85, https://doi.org/10.1016/j.jcp.2013.01.050.

91. M. Dumbser and E. F. Toro, "A Simple Extension of the Osher Riemann Solver to Non-conservative Hyperbolic Systems," *Journal of Scientific Computing* 48, no. 1 (2011): 70–88, https://doi.org/10.1007/s10915-010-9400-3.

92. C. Parés and M. Castro, "On the Well-Balance Property of Roe's Method for Nonconservative Hyperbolic Systems. Applications to Shallow-Water Systems," *ESAIM. Mathematical Modelling and Numerical Analysis* 38, no. 5 (2004): 821–852, https://doi.org/10.1051/m2an:2004041.

93. A. Harten and S. Osher, "Uniformly High-Order Accurate Nonoscillatory Schemes," *I. SIAM Journal on Numerical Analysis* 24, no. 2 (1987): 279–309, https://doi.org/10.1137/0724022.

94. M. Dumbser and E. F. Toro, "On Universal Osher-Type Schemes for General Nonlinear Hyperbolic Conservation Laws," *Communications in Computational Physics* 10, no. 3 (2011): 635–671, https://doi.org/10.4208/cicp.170610.021210a.

95. V. Caleffi and A. Valiani, "Well Balancing of the SWE Schemes for Moving-Water Steady Flows," *Journal of Computational Physics* 342 (2017): 85–116, https://doi.org/10.1016/j.jcp.2017.04.031.

96. J. Sturdy, J. K. Kjernlie, H. M. Nydal, V. G. Eck, and L. R. Hellevik, "Uncertainty Quantification of Computational Coronary Stenosis Assessment and Model Based Mitigation of Image Resolution Limitations," *Journal of Computational Science* 31 (2019): 137–150, https://doi.org/10.1016/j.jocs.2019.01.004.

97. J. Feinberg and H. P. Langtangen, "Chaospy: An Open Source Tool for Designing Methods of Uncertainty Quantification," *Journal of Computational Science* 11 (2015): 46–57, https://doi.org/10.1016/j.jocs.2015.08.008.

98. D. F. Young, N. R. Cholvin, and A. C. Roth, "Pressure Drop Across Artificially Induced Stenoses in the Femoral Arteries of Dogs," *Circulation Research* 36, no. 6 (1975): 735–743, https://doi.org/10.1161/01.RES.36.6.735.

99. B. K. Koo, A. Erglis, J. H. Doh, et al., "Diagnosis of Ischemia-Causing Coronary Stenoses by Noninvasive Fractional Flow Reserve Computed From Coronary Computed Tomographic Angiograms: Results From the Prospective Multicenter DISCOVER-FLOW (Diagnosis of Ischemia-Causing Stenoses Obtained via Noninvasive Fractional Flow Reserve) Study," *Journal of the American College of Cardiology* 58, no. 19 (2011): 1989–1997, https://doi.org/10.1016/j.jacc.2011.06.066.

100. J. K. Min, D. S. Berman, M. J. Budoff, et al., "Rationale and Design of the DeFACTO (Determination of Fractional Flow Reserve by Anatomic Computed Tomographic Angiography) Study," *Journal of Cardiovascular Computed Tomography* 5, no. 5 (2011): 301–309, https://doi.org/10.1016/j.jcct.2011.08.003.

101. B. L. Nørgaard, J. Leipsic, S. Gaur, et al., "Diagnostic Performance of Noninvasive Fractional Flow Reserve Derived From Coronary Computed Tomography Angiography in Suspected Coronary Artery Disease: The NXT Trial (Analysis of Coronary Blood Flow Using CT Angiography: Next Steps)," *Journal of the American College of Cardiology* 63, no. 12 (2014): 1145–1155, https://doi.org/10.1016/j.jacc.2013.11.043.

102. S. Fiorentini, L. Saxhaug, T. Bjåstad, E. Holte, and H. Torp, *3D Tracking Doppler for Improved Quantitative Blood Flow Assessment of Coronary Arteries* (Washington, DC: IEEE, 2017), 1–4, https://doi.org/10.1109/ULTSYM.2017.8092469.

103. J. Schwitter, T. DeMarco, S. Kneifel, et al., "Magnetic Resonance–Based Assessment of Global Coronary Flow and Flow Reserve and Its Relation to Left Ventricular Functional Parameters: A Comparison With Positron Emission Tomography," *Circulation* 101, no. 23 (2000): 2696–2702, https://doi.org/10.1161/01.cir.101.23.2696.

104. L. Itu, P. Sharma, K. Ralovich, et al., "Non-Invasive Hemodynamic Assessment of Aortic Coarctation: Validation With In Vivo Measurements," *Annals of Biomedical Engineering* 41, no. 4 (2013): 669–681, https://doi.org/10.1007/s10439-012-0715-0.

105. Y. Huo, M. Svendsen, J. S. Choy, Z. D. Zhang, and G. S. Kassab, "A Validated Predictive Model of Coronary Fractional Flow Reserve," *Journal of the Royal Society Interface* 9, no. 71 (2012): 1325–1338, https://doi.org/10.1098/rsif.2011.0605.

106. D. Bessems, "On the Propagation of Pressure and Flow Waves Through the Patient Specific Arterial System," 2007, https://doi.org/10.6100/IR629017.

Supporting Information

Additional supporting information can be found online in the Supporting Information section.